Review article

Masfer H. Alkahtani*, Fahad Alghannam, Linkun Jiang, Abdulrahman Almethen, Arfaan A. Rampersaud, Robert Brick, Carmen L. Gomes, Marlan O. Scully and Philip R. Hemmer

Fluorescent nanodiamonds: past, present, and future

https://doi.org/10.1515/nanoph-2018-0025
Received February 22, 2018; revised April 27, 2018; accepted May 14, 2018

Abstract: Multi-color fluorescent nanodiamonds (FNDs) containing a variety of color centers are promising fluorescent markers for biomedical applications. Compared to colloidal quantum dots and organic dyes, FNDs have the advantage of lower toxicity, exceptional chemical stability, and better photostability. They can be surface functionalized by techniques similar to those used for other nanoparticles. They exhibit a variety of emission wavelengths from visible to near infrared, with narrow or broad bandwidths depending on their color centers. In addition, some color centers can detect changes in magnetic fields, electric fields, and temperature. In this article review, we will discuss the current trends in FND's development, including comparison to the early development of quantum dots. We will also highlight some of the latest advances in fabrication, as well as demonstrations of their use in bioimaging and biosensing.

Keywords: fluorescent nanodiamonds; imaging; sensing; color centers; fluorescent probes.

***Corresponding author: Masfer H. Alkahtani,** Texas A&M University, College Station, TX 77843-4242, USA; and Center for Quantum Optics and Quantum Informatics, KACST, Riyadh 11442, Saudi Arabia, e-mail: masfer84@tamu.edu, mqhtani@kacst.edu.sa
Fahad Alghannam and Abdulrahman Almethen: Texas A&M University, College Station, TX 77843-4242, USA; and Center for Quantum Optics and Quantum Informatics, KACST, Riyadh 11442, Saudi Arabia
Linkun Jiang and Robert Brick: Texas A&M University, College Station, TX 77843-4242, USA
Arfaan A. Rampersaud: Columbus NanoWorks Inc., 1507 Chambers Rd, Columbus, OH 43212, USA
Carmen L. Gomes: Mechanical Engineering Department, Iowa State University, Ames, IA 50011, USA
Marlan O. Scully: Texas A&M University, College Station, TX 77843-4242, USA; and Baylor University, Waco, TX 76798, USA
Philip R. Hemmer: Texas A&M University, College Station, TX 77843-4242, USA; Center for Quantum Optics and Quantum Informatics, KACST, Riyadh 11442, Saudi Arabia; Electrical and Computer Engineering, Texas A&M University, College Station, TX 77843-3128, USA; and Zavoisky Physical-Technical Institute, Federal Research Center "Kazan Scientific Center of RAS", Kazan, Russia

1 Introduction

Over the past decades, efforts have been focused on the development of fluorescent nanoparticles to analyze complex biological processes, as well as to track and localize individual drugs, proteins, nucleic acids, and small molecules [1–5]. Ideal fluorescent nanoparticles should exhibit most, if not all, of the following features: (1) high sensitivity, down to the single molecule level, (2) high spatial resolution (with correspondingly small size at the nanoscale), (3) high molar absorption coefficient at the excitation wavelength with high fluorescence quantum yield, (4) absence of blinking and photo bleaching for real-time imaging, (5) robust surface chemistry, (6) biocompatibility, and (7) lack of toxicity. Furthermore, a suitable fluorescent marker should be conveniently excitable and detectable in the biological transparency window to avoid simultaneous excitation of endogenous fluorescent molecules, such as blood constituents, cofactors, and water. Unfortunately, most fluorescent markers do not possess all of these features.

The most widely used fluorescent markers are organic dyes, such as rhodamine, coumarin, and cyanine dyes, and their derivatives. Within the group of dyes, we could also include fluorophores that are part of a protein's structure (such as phycobiliproteins and fluorescent proteins that can be genetically encoded) [6]. While most organic dyes exhibit moderate to high quantum yields, many are photolabile and undergo photobleaching during continuous excitation. The Stokes shift (the difference between the spectral positions of the maxima of the absorption and emission spectra) [7] for most fluorescent dyes are often very small [8], which poses problems such as cross-talk

between different dye molecules. Additionally, the intensity of the fluorescence depends on the local environment and can be influenced by pH, hydrophobicity, temperature, and solvent [7]. The only fluorophore that is FDA approved for clinical use is the organic dye indocyanine green (ICG) [9]. However, ICG suffers from very low fluorescence quantum yield [10, 11], limited stability, and binding to plasma proteins [12].

Fluorescent nanoparticles overcome some of the limitations of organic dyes, such as quenching and environmental factors, and can be separated into a few distinct groups, including quantum dots [13, 14], highly fluorescent semiconducting polymer dots [15], ultrabright fluorescent silica particles [16], upconverting nanoparticles [17–19], gold nanoparticles [20], carbon dots [21], as well as a large group that can be described as dye-doped polymeric nanoparticles [20]. Quantum dots (QDs) are clusters of semiconductor nanocrystals, created from II/VI and III/V elements, that display size-dependent luminescence [13, 14]. QDs absorb photons in the ultraviolet region, and then emit photons at longer wavelengths, in a size-dependent fashion. Relative to organic dyes, QDs exhibit non-quenching fluorescence, with large Stokes shifts, high fluorescence quantum yields, and can be made in an ultrasmall size (<2 nm) for single molecule imaging [13, 14]. However, QDs have not gained broad and substantial acceptance in the biological sciences due in part to the known toxicity of the Cd that forms the core of most QDs. While it is possible to coat the Cd core with a protective shell, their biocompatibility is still debated [13, 22], largely due to concerns about leaking of Cd^{2+}, and cytotoxic surface ligands [23]. On the other hand, upconverting nanoparticles (UCNPs) and gold nanoparticles have good biocompatibility and photostability, but show low fluorescence quantum efficiency [17, 18, 24, 25]. Due to space limitations, UCNPs, gold nanoparticles, carbon dots, and dye-doped polymeric nanoparticles will not be discussed further in this review.

Fluorescent nanodiamonds (FNDs), owing to their unique optical and chemical properties, are proposed to be the best alternative probes that can meet the ideal fluorescent marker's criteria. In this section, we will compare FNDs to commonly used QDs in terms of optical properties, photostability, and biocompatibility.

1.1 FNDs and QDs optical properties

FNDs and QDs share important optical, chemical, photochemical, and photophysical properties that make them excellent fluorescent markers. However, they have completely different electronic structures. QDs have delocalized electrons whose wavefunction can extend to the surface, while FNDs have color center defects that act like isolated atoms or molecules in a solid host. Therefore, photoluminescence of FNDs originates from local defects (color centers) in nanodiamond crystals and, at least in principle, is not expected to be strongly affected by crystal size until the nanodiamond size becomes less than 5 nm.

FNDs bright and photostable photo-luminescence cover a wide range of the VIS to NIR spectrum; for instance, blue emission for N3 center, green emission for H3 (N2V) complex, red-NIR emission for nitrogen-vacancy (NV center), silicon-center (SiV), germanium-vacancy (GeV), tin-vacancy (SnV), and nickel center (Ni) color centers [26–31], as shown in Figure 1A [32]. Here, it is important to note that new color centers are being discovered on a yearly basis, as only a fraction of the periodic table has so far been implanted into diamond [34]. Many of the new color centers are narrowband as preferred for biomarkers, especially for large-atom implantation.

Of these color centers, the NV center is the most extensively studied type of fluorescent diamond centers and has been well characterized for its photophysics, as well as its use in biological settings. Unless specifically stated, the remaining discussion on NVs is taken largely from the recent NV-center literature. The brightness of FNDs depends on the average number of emitting color centers per particle [35]. Recently, the brightness of these FNDs and color centers stability (especially for NV center) have been optimized as a function of size [36]. Accordingly, irradiated 100 nm FNDs (with NV color centers) are 12 times brighter than a conventional organic dye (Auto 532 dye) [36]. For small FNDs, with a size less than or equal to 20 nm, brightness will decrease by about two orders of magnitude compared to that for 100 nm FNDs. Recent efforts have been made to optimize the brightness stability of small NDs down to 10 nm (almost single emitter), and they are commercially available for biomedical applications [36].

The brightness of QDs is much higher than FNDs [28] and the emission spectra of QDs are tunable by particle size, as shown in Figure 1B [13, 33]. The quantum confinement effect is especially relevant when the size of the QDs crystals becomes smaller than the Bohr radius (for example ~5 nm for CdSe) and causes the energy of the optical transitions to be dependent on the properties of the shell material, and strongly on their size [37–39]. As a result, the photoluminescence of QDs is very sensitive to their surface states; fluorescence transduction is based on the principle that chemical or physical interactions occurring at the surface of the QDs change the efficiency of the radiative recombination, leading to photoluminescence

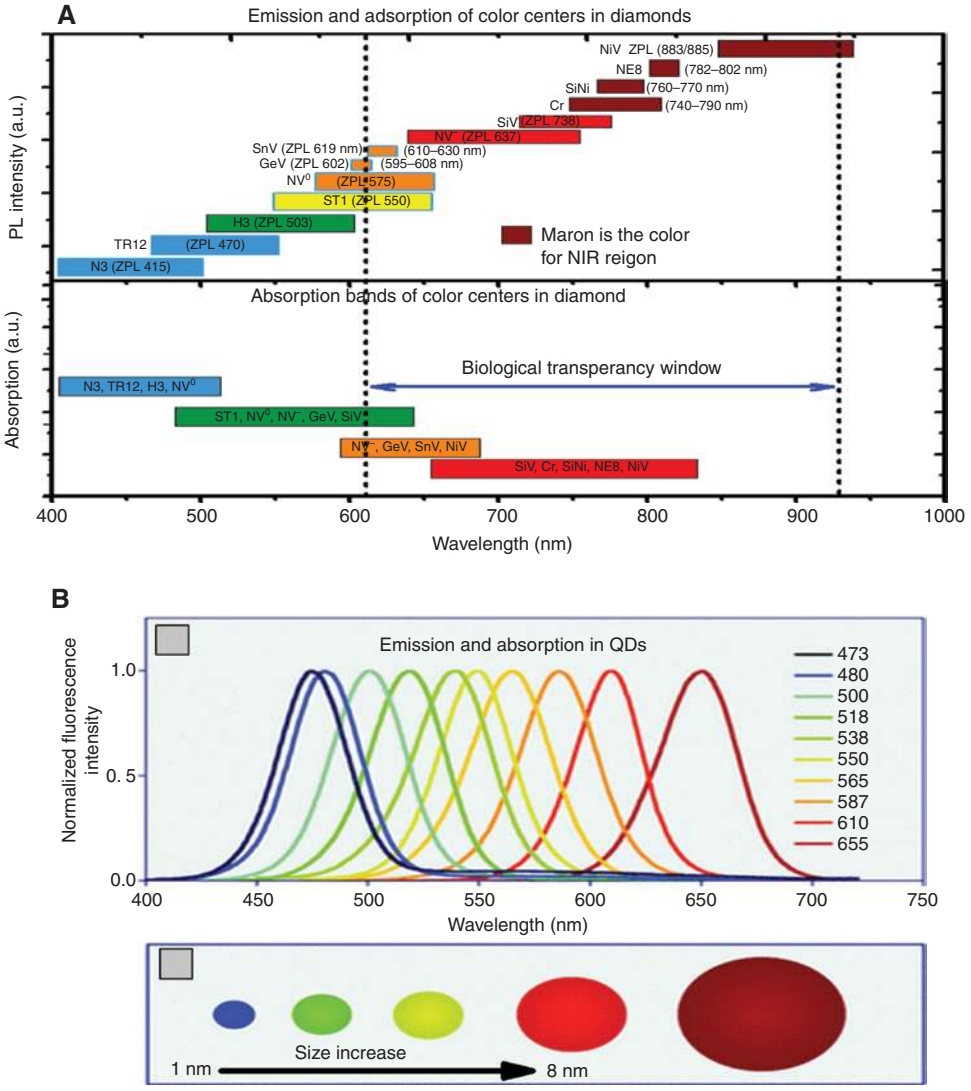

Figure 1: Optical properties of FNDs and QDs.
(A) Absorption and emission bands of most of the color centers in diamonds. Adapted from [32]. (B) Quantum dot emission wavelength as a function of size. Adapted from [33].

blinking [40]. Recently, there have been reports of ultrasmall QDs with suppressed blinking [41], but these were not reproducible and later retracted [42].

1.2 FNDs versus QDs biocompatibility

QDs biocompatibility has been extensively investigated and is still debated [23, 43]. Assessments of QDs in living cells using *in vitro* experiments have been reported in [44]. QDs have shown an increase in the percentage of cell deaths as the concentration increases. A recent study based on cell viability indicates that toxicity is closely correlated with quantum dot surface properties (including shell, ligand, and surface modifications) [45]. Safety concerns are still high for using the most efficient QDs structure (CdSe core covered by ZnS and further covered by ZnS/SiO_2 multiple shells), because the expected leakage of cadmium ions results in cytotoxicity [23]. Toxicity, based on cell death measurements, was minimized to about 20% of its original value by coating the surface of QDs with poly(ethylene glycol) (PEG), as shown in Figure 2A [44]. To avoid cytotoxic materials in general, possible alternatives to classical QD labels could be InP or InGaP [49, 50] of III/V group semiconductors, which are currently available commercially. However, these nanoparticles are much more difficult to synthesize and do not display photoluminescence intensities comparable with classical QDs, such as CdSe.

Recently, efforts have been focused on capping the surface of QDs to improve biocompatiblity. For example,

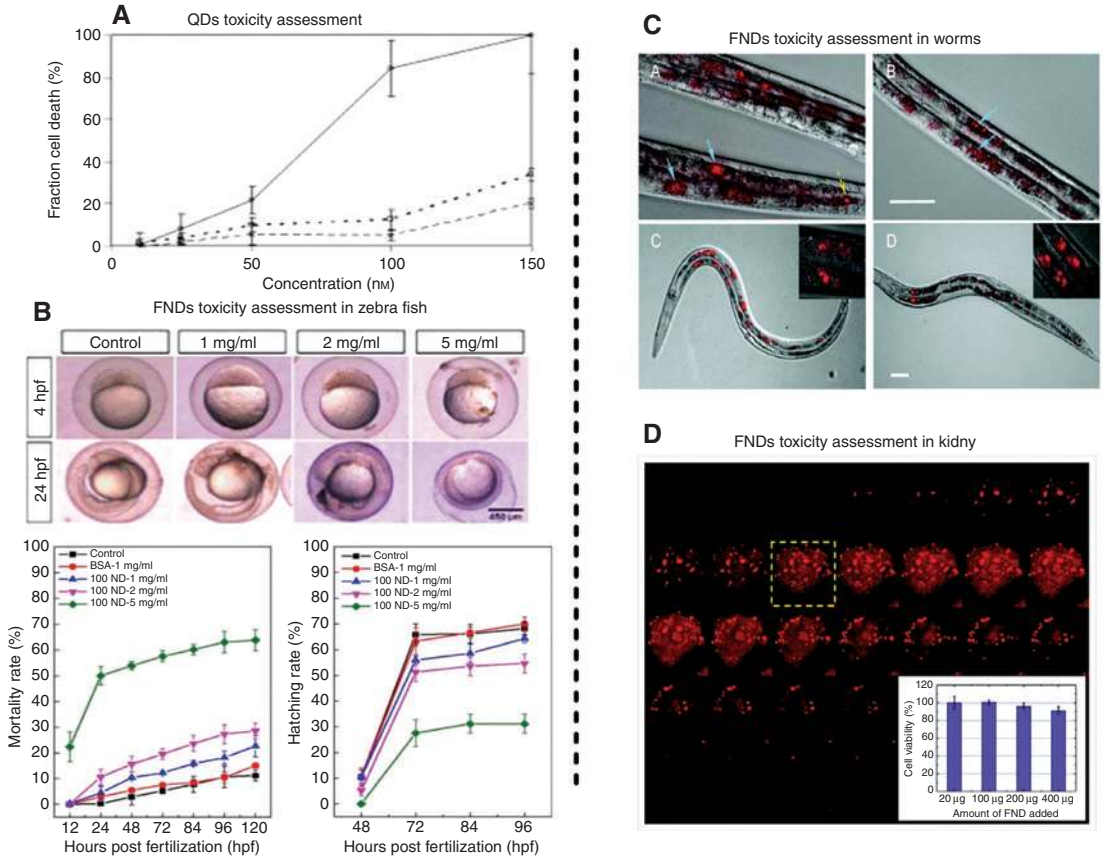

Figure 2: An illustration of toxicity levels of QDs and FNDs in living organisms.
(A) Toxicity assessment of cell exposed to QDs for 4 h. The upper curve represents pure QDs without surface modifications. The other curves illustrate QDs with PEG coating at different concentrations (750- and 6000-Mw PEG-substituted QDs). Adapted from [44]. (B) Zebrafish embryos development stages with various concentrations of nanodiamond for different periods at 4-h post-fertilization (hpf) and 24 hpf (upper image in Figure 2B). Mortality and hatching of zebrafish embryos as a function of the NDs concentrations (lower image in Figure 2B). Adapted from [46]. (C) Images of worms fed with FNDs coated with BSA (bovine serum albumin) and DOX (doxorubicin). Insets: 100× magnified images of the FNDs within the intestinal cells. Adapted from [47]. (D) Optical images of a single human kidney cell after fluorescent nanodiamond uptake. The red spots are the FNDs. Inset: Toxicity assessments of showing the survival percentage of the kidney cells versus the FNDs doses. Adapted from [48].

a parallel comparative study including *in vitro* and *in vivo* experiments was done on the toxicity of quantum dots synthesized by different techniques and with different surface engineering [51]. Specifically, these experiments were done on living cells in culture, and on a group of mice, using three groups of QDs. These different QDs groups are prepared as follows: QDs encapsulated by an amphiphilic polymer (denoted as QDs-1), QDs surface engineered by glutathione-mediated ligand exchange (denoted as QDs-2), and QDs prepared by a coprecipitation approach in the aqueous phase that produces a mercaptopropionic acid capped surface (denoted as QDs-3). It was found that QDs-1 encapsulated with an amphiphilic polymer have the lowest toxicity in both cellular and mice experiments. Furthermore, QDs-1 exhibits less adverse effects on cell proliferation and DNA fragmenting, while both QDs-2 and QDs-3 show obvious cell damage [51]. This study suggests that encapsulation methods play vital roles in the acute toxicity profiles of QDs. In general, toxicity associated with QDs is a big concern in biological applications.

In contrast to QDs, the toxicity of FNDs is entirely related to the surface purity. For example, nanodiamonds produced by detonation (DNDs) have been reported to have strong anti-bacterial properties, if not well cleaned [52]. However, aggressively cleaned FNDs do not show this behavior. Additionally, functionalization can suppress toxicity of uncleaned DNDs, for example strong bonds (C-C bonds) can be created between the graphitic shell and the surface functional groups following Diels–Alder reactions [53] and diazonium chemistry [54].

However, it is preferable to remove the graphitic shell for quantum efficiency and phototoxicity considerations. This is normally done with aggressive oxidation both in liquid (boiling in acids) and in air at temperatures above

500°C [55]. Once the surface has been cleaned to expose a pristine diamond surface, there are a number of functionalization strategies that have been applied. For example, one approach is to reduce all carboxyl (-COOH) groups to hydroxyl (-OH). From this, a silane linkage can be made [56], or alternatively nitrogen can be attached directly to the surface carbon, serving as a basis for linkers like PEG, antibodies, proteins, DNA, etc. [57–59].

Recently, Havlik et al. developed a synthetic method to replace the carboxylic group on nanodiamonds (NDs) surface by fluorine using selective sp^3-based radical chemistry [60]. This surface modification produces nanodiamonds with a highly hydrophilic interface with mixed C-F and C-OH terminations. These dual terminations on NDs surface suppress hydrophobic interactions, which cause NDs agglomeration in solutions. Furthermore, fluorination of NDs leads to surface band-bending that stabilizes shallow fluorescent NV center for small size FNDs (especially size <100 nm) [60]. All these surface advanced modifications make NDs suitable for a variety of biomedical applications.

Toxicity assessments, after surface preparation, have been performed on FNDs by *in vitro* and *in vivo* experiments. The most sensitive experiments were done by Cheng and coworkers [46] who conducted toxicity tests of nanodiamonds (NDs) on the zebrafish embryo model *in vivo*. This model is especially sensitive to toxicity at critical stages of embryo development. They found that for ND concentrations below 1 mg/ml, even in the critical stage, zebrafish embryos exhibit similar development as compared to the control groups, as shown in Figure 2B. However, at higher concentrations, the NDs affect the zebrafish embryos at the Pharyngula stage, as shown in Figure 2B. The results suggested that NDs are safe as a drug delivery agent for concentrations below 1 mg/ml. In this study, a significant toxicity was observed only for very high ND concentration, above 5 mg/ml, where an increase in the mortality rate of zebrafish embryos (to 60%) and a decrease in hatching rate (to 20%) was seen, as shown in Figure 2B [46]. In earlier work, FNDs were also fed to more than 600 worms (C. Elegans) ~600 worms at a dose of the range of ~3 ng/worm or $\sim 1 \times 10^6$ particles/worm. This amount of FNDs did not cause any detectable stress to the worms for several days, as shown in Figure 2C [47]. Upon microinjection of the worms with FNDs, some were passed along to offspring without any apparent effect on development. Another early study showed only a modest decrease of cell viability at a FND dose of very high dose of 400 mg/ml corresponding to 10^{11} particles per ml after uptake by 293 T kidney cells, as shown in Figure 2D [48]. Recently, FNDs have been injected into groups of mice for more than 5 months at a dosage of up to 75 mg/kg body mass and shown no evidence of toxicity, neither in the living animals, nor in the histopathological examinations [61]. In another important study on nanodiamonds toxicity assessment, 0.002–0.05 wt% of NDs in solution hydrosols were given to mice instead of water for 6 months and showed no significant effects on growth rates, organ weights, or reproductive rates for at least 3 generations [62]. For more extensive discussion of NDs toxicity including those with cleaned and uncleaned surfaces a recent review is recommended [55].

1.3 Challenges for fluorescent nanodianonds

FNDs exhibit unique optical and chemical properties, as well as exceptional biocompatibility as discussed above. However, there are still challenges that can limit short and long-term interaction of nanodiamonds with living organisms. These include colloidal stability, specific targeting of structures in biological samples, and brightness against auto-fluorescence in commercial microscopes, especially those using filters specifically designed for particular dyes.

Successful strategies have been developed to achieve stable aqueous dispersions of NDs produced from commercial detonation nanodiamonds or crushed/milled high pressure high-temperature (HPHT) diamonds [22, 62–64]. Briefly, as outline in review paper [22], the problem arises when crushed NDs (HPHT) or DNDs are irradiated with an ion beam and annealed at high temperature in a vacuum to create color centers. Annealing at high temperature results in a graphitic shell formed on the surface of the NDs which is responsible for the instability. However, this can be removed by a combination of dry and wet oxidation (mixture of nitric and sulfuric acids). This oxidization produces carboxylic groups on the surface of the NDs which increase the colloidal stability and allows further functionalization for specific bio-conjugations. Furthermore, oxidization of the surface of NDs allows covalent modifications that have been proposed to improve stability in biological environments as well as to increase the loading capability for the delivery of therapeutic cargos [22, 63].

As mentioned above, another challenge facing the use of FNDs in biological imaging is the degree of nanodiamond brightness. This was studied in detail in reference [28] and is summarized in Figure 3A which compares signal to (autofluorescence) background ratio (SBR) of NDs to organic dyes and QDs. To keep this in perspective, Figure 3B shows photostability for the same fluorescent emitters to illustrate the tradeoff in brightness versus bleaching rate. Some of the poor SBR performance of NV is due to a mismatch of

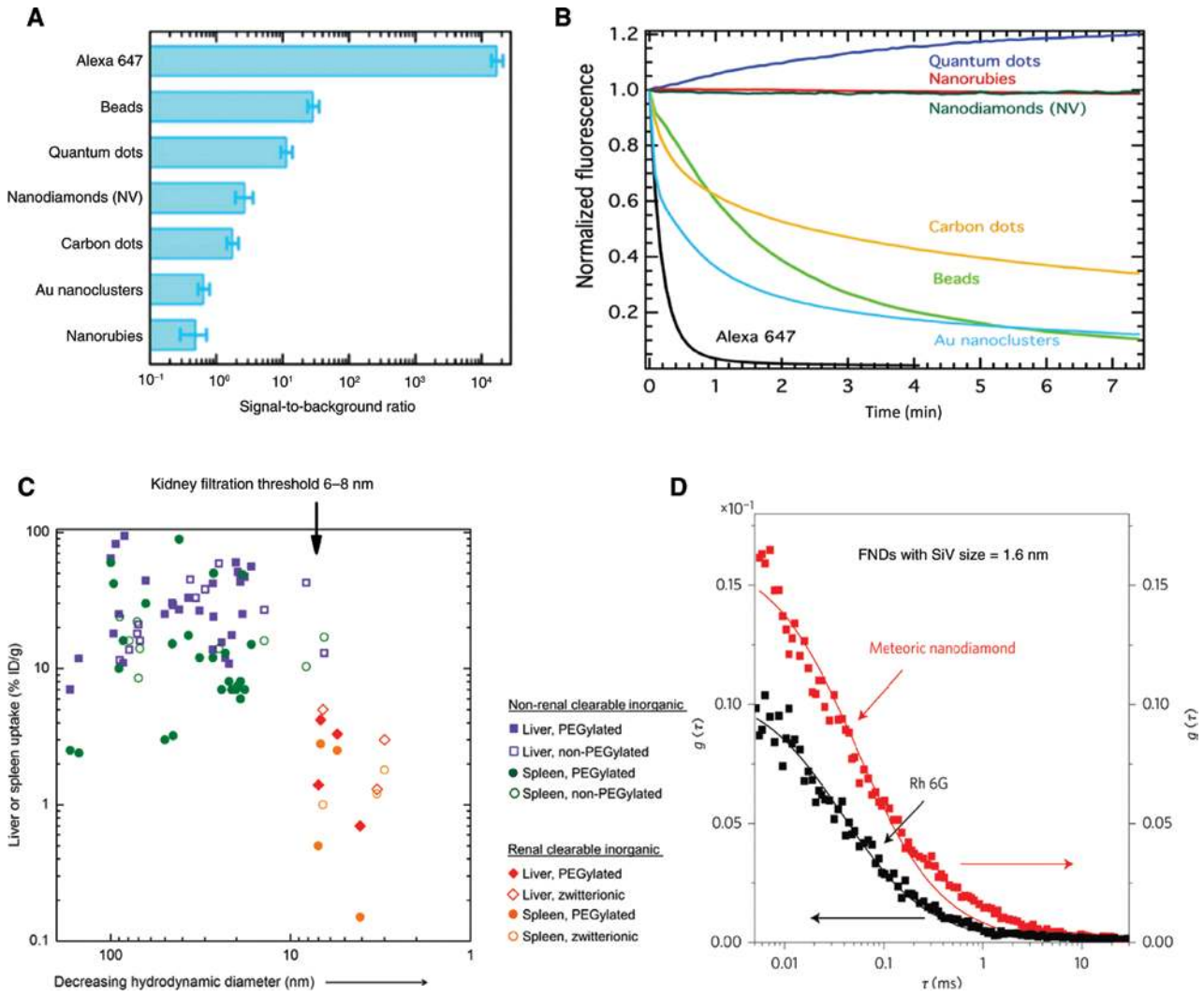

Figure 3: A Brightness and photostability of FNDs compared to other fluorescent nanoparticles. Also a demonstration of kidney filtration threshold of small nanoparticles.
(A) Signal-to-noise ratio comparison of different fluorescent materials performed on a commercial microscope (Olympus IX83-wide field fluorescence microscope). Adapted from [28]. (B) Normalized fluorescence emission intensity as a function of time for different fluorescent probes under continuous excitation. Adapted from [28]. (C) Liver, spleen, and uptake of representative nonrenal clearable inorganic NPs and renal-clearable inorganic NPs in mice following intravenous injection. Adapted from [65]. (D) The measured autocorrelation function (red symbols) to estimate the effective size of fluorescent nanodiamonds with SiV color center of 1.6 ± 0.2 nm when using 0.6 nm as a reference for the hydrodynamic radius for Rhodamine 6G in water. Adapted from [66].

excitation, emission, and dichroic filter sets. To address this, Philipp Reineck et al. recently studied the influence of different optical filters for FNDs and came up with suitable filter combinations that can improve the signal to noise ratio of FNDs in commercial microscopes [28].

Finally, while the exceptional physico-chemical stability of diamonds is considered an advantage for imaging, it may be a concern for medical applications if there is accumulation in the tissue. This was addressed by a recent study [65] which showed that fluorescent nanoparticles of size greater 8 nm can be trapped in the body tissue. In contrast, particles of smaller sizes (including all surface chemistry) can be rapidly eliminated from the body via kidneys (and liver) but can still passively target a tumor with high efficiency. Note that in this study, fluorescent nanoparticles are divided to nonrenal clearable inorganic NPs (above the kidney filtration threshold 6–8 nm) and renal-clearable ones (below the kidney filtration threshold 6–8 nm), as shown in Figure 3C, where it was noted that shape and surface chemistry can modify the size threshold. Fortunately, ultrasmall fluorescent nanodiamonds (size less than 2 nm as shown in Figure 3D) have been reported in the literature [66]. Later we will discuss how such ultrasmall ND particles might soon be mass-produced.

2 Bio-applications of FNDs

Drug delivery is one of the earliest bio-medical applications of nanodiamonds (NDs) that has been investigated. Also, clinical applications of non-fluorescent DND nanodiamonds are the most recent technology in bio-applications. Initially, non-fluorescent nanodiamonds were used.

2.1 Non-fluorescent nanodiamonds for drug delivery

Early studies on the use of nanodiamonds as drug delivery vehicles were reported by the group of Ho in 2007 [67]. These studies showed that the chemotherapeutic agent doxorubicin (DOX) could be passively absorbed onto the surface of non-fluorescent nanodiamonds to create nanodiamond-drug complexes (NDX) then delivered into cancer cells with preserved efficacy, as well as slow and sustained DOX release [67, 68]. The NDX treatment overcomes a problem seen with drug-resistant tumors in which transporter proteins facilitate the efflux of drug compounds out of the cell, markedly decreasing, or precluding treatment efficacy. A mechanism of how these nanodiamonds act to circumvent drug resistance is shown in Figure 4A [69]. Similarly, absorption and delivery of other drugs have been reported including, anticancer agents mitoxantrone (MTX), cisplatin, 4-hydroxytamoxifen (4-OHT), and purvalanol A [70–73], an anti-inflammatory drug dexamethasone [73], and the diabetes drug insulin [74].

In preclinical experiments, the NDX complex was shown to inhibit tumor growth in both murine LT2-Myc liver tumor and 4T1 mammary tumor without affecting normal tissues [68]. Figure 4B shows that treatment with 100 μg of a Dox equivalent of either free Dox or NDX effectively inhibited liver tumor growth, with a measurable preference for NDX. ND with Dox has decreased the percentage of mice with tumors, after treatment, to less than 50% and increased the survival probability over a long period of time as shown in Figure 4C, D. In additional safety studies, NDX was found not to elicit myelosuppression, which is an unwanted side effect of free DOX chemotherapy underlying patient mortality.

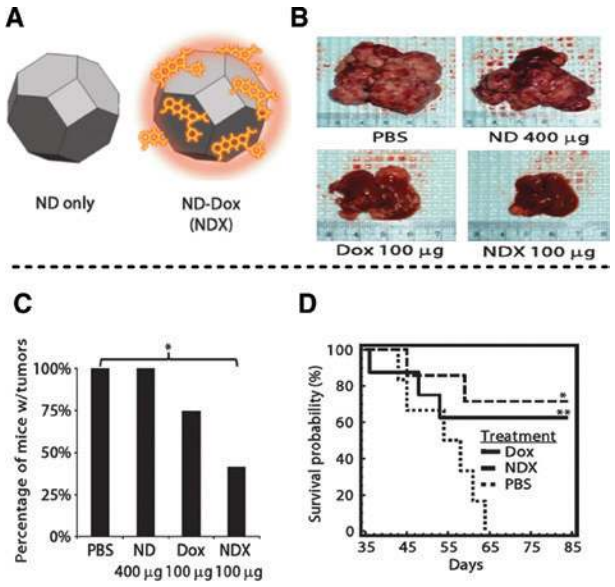

Figure 4: An illustration of using nanodiamonds as drug delivery vehicles.
(A) Scheme of ND and ND with DOX(NDX). (B) Images of livers/tumors from treated mice with PBS, ND 400 μg, Dox 100 μg, and ND-Dox 100 μg. (C) Percentage of mice exhibiting macroscopic tumor nodules (defined as >1 mm). *$p < 0.03$. (D) Kaplan-Meier survival plot for LT2-Myc mice treated with PBS ($n = 5$), DOX (100 μg; $n = 8$), or NDX (100 μg of Dox equivalent; $n = 7$) by tail vein injection every 7 days. *$p < 0.03$; **$p < 0.06$. Adapted from [68].

2.2 Non-fluorescent nanodiamonds in Root canal therapy (RCT)

RCT is a common treatment used to address infected pulp tissue and protect the tooth against future reinfection in order to preserve its normal function. The current material used in RCT obturation is gutta percha (GP), which is generally made of zinc oxide and other materials [75]. Commonly used GPs are limited by microleakage, allowing fluids and bacteria to access the treated root canal. In addition, GPs also have suboptimal mechanical properties, which can cause buckling during obturation [76, 77].

In a recent achievement, Ho and his co-authors embedded GPs with nanodiamonds (NDs) to form GPs-ND composition that has shown better performance for root canal filling [78] than GP alone, as shown Figure 5A. GPs-NDs demonstrated improved tensile strength and resistance to elongation during loading into the obturation system compared with unmodified GP, as shown in Figure 5B, C. In clinical application, successful results of GPs-NDs treatment were observed, and enhanced lesion healing was confirmed in the GPs-NDs-treated patients [78].

2.3 Non-fluorescent nanodiamonds in bone growth

Nanodiamonds have been used for bone and tissue implants [55] several years ago. Recently, Ho and his co-authors [79] proposed an innovative treatment of cleft lip and/or palate (CLP), which is caused by failure of fusion between maxillary and nasal processes [80, 81].

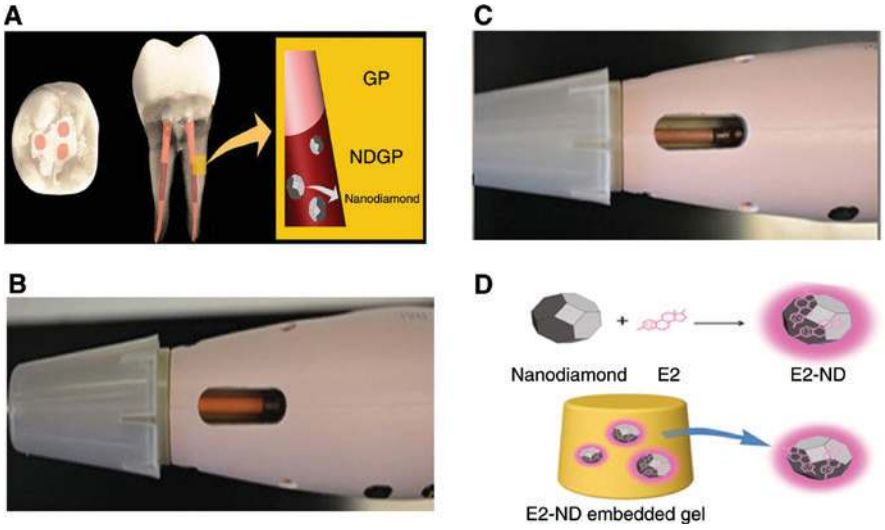

Figure 5: Clinical applications of nanodiamonds.
(A) An illustration of NDGP in the middle third of the root canal and unmodified GP in the apical and coronal thirds of the root canal-treated tooth. (B) A view of unmodified GP in the dispensing unit. (C) A view of NDGP in the dispensing unit. Adapted from [78]. (D) A schematic of E2/ND complex embedded within a hydrogel matrix. Adapted from [79].

This defect is normally corrected by surgery, but there is a strong tendency to rebound to the original shape, resulting in relapse [82, 83].

To overcome these limitations, a nanodiamond–hydrogel (ND/G) complex vehicle was developed as illustrated in Figure 5D. Estrogen, 17β-estradiol (E2), which has proven bone-building properties, is then incorporated within this vehicle. It was found that the E2/ND/G complex substantially reduced post-expansion relapse by nearly three-fold compared to E2 alone. In addition, the E2/ND/G complex produced greater bone volume by two-fold or higher compared with the control group.

2.4 Fluorescent nanodiamonds for drug delivery

In general, FND are normally made from crushed high-pressure high-temperature (HPHT) bulk diamonds or in some cases chemical vapor deposition (CVD)-grown nanodiamonds, as these are typically much brighter than detonation diamonds. Therefore, for image monitored drug delivery non-detonation FNDs are preferred as discussed in two studies [84–86]. In the second of these studies, FNDs were coated with biopolymers and proteins to ensure colloidal stability and conjugated to DOX molecules for treatment of cancer cell lines. The FNDs-DOX complex uptake and drug release process in a cancer cell is illustrated in Figure 6A. The FNDs-DOX complex was photostable inside living cells, as shown in Figure 6B [85]. Figure 6C shows that the fluorescence of the NV color center in diamond overlaps with emission of doxorubicin, but this can be subtracted to show the NV centers alone. Significant amounts of DOX were released from ND carriers in these studies and in other experiments, FNDs-DOX have shown efficient tumor inhibition of human cancer cells over time, as shown in Figure 6C, D [85]. Furthermore, tumor luminescence decreased to very low percentages over time, as shown in Figure 6F, which indicates the cancer fighting effect of FNDs-DOX in human cancer [85]. All the advantages above-mentioned indicate that FNDs are intriguing candidates as delivery platforms for chemicals and antibodies.

3 Tracking of fluorescent nanodiamonds inside living cells

Real-time tracking of dynamic biological processes in living organisms such as single motor protein stepping [87, 88], DNA polymerization [89], and cell membrane motility [90, 91] has been dramatically improved by the use of photostable fluorescent markers. Dynamic fluorescent probe tracking involves monitoring the position and distribution of a finite number of individual fluorescent probes over time with high spatial resolution. Conventional fluorescent markers including organic dyes, QDs, and UCNPs have been used for single particle tracking; however, previously discussed limitations such as photostability, cytotoxicity, and low quantum efficiency reduce the sensitivity of real-time tracking [5, 92–95]. Fluorescent nanodiamonds have been shown to be the best candidates for long

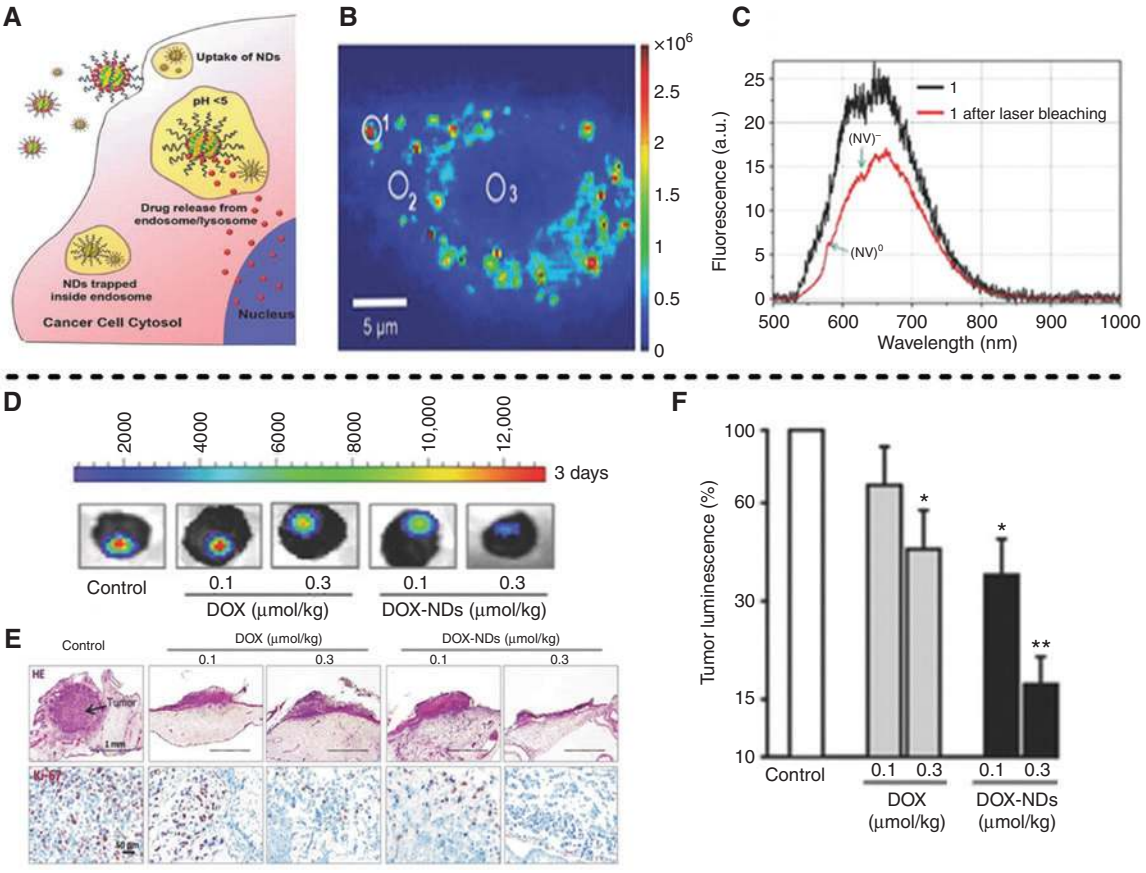

Figure 6: Biological applications of fluorescent nanodiamonds in drug delivery.
(A) Demonstration of living cell uptake and drug release process of DOX-ND. (B) Fluorescence spectra of fluorescent DOX-NDs inside living (A549) cells. (C) Black curve represents the overlapping emission spectra of DOX and NV centers. The red curve illustrates the emission spectrum after laser bleaching of the DOX emission showing a clear NV center spectrum with NVo and NV peaks at 575 and 638 nm, respectively. (D) Human cancer xenografts treated with NDs-DOX after 3 days. (E) Breast cancer cells treated with DOX-ND over time. NDs-DOX treatment reduced the cancer cell proliferation in a dose-dependent manner. (F) Luminescence imaging analysis of tumor xenograft growth after 3 days treatment by NDs-DOX. *$p < 0.05$, **$p < 0.01$. Adapted from [85].

term single particle tracking applications owing to their photostable and bright color centers and extraordinary biocompatibility [96–98]. Hollenberg et al. demonstrated tracking of individual fluorescent NVs in nanodiamonds in human HeLa cells. By using the spin and magnetic sensing properties of the NV, they measured not only location, but also orientation of NV nanodiamonds [98]. Furthermore, using the spin properties of individual NVs as fingerprints, it is possible to simultaneously track multiple particles, in principle even for spacing less than the diffraction limit.

For these studies, they used 45 nm fluorescent nanodiamonds that were uptaken by human HeLa cells via co-incubation, as shown in Figure 7A. The NV center has an $S=1$ spin ground state, which is split into a pair of sublevels ($m_s=\pm1$, and $m_s=0$) with a zero-field splitting near $D=2.87$ GHz. This splitting is due to spin-orbit interactions and the local diamond crystal field, as shown in Figure 7B, and is therefore slightly different for each NV [99], which gives the distinguishability discussed above in the absence of an externally applied magnetic field ($B_0=0$). In particular Hollenberg et al. [98], track and identify two NV color centers (NV-1a and NV-1b) with different strain splitting inside the HeLa living cell, as shown in Figure 7C [98]. In addition, by applying a weak magnetic field, the orientation of the NV spin quantization axis relative to the applied magnetic field can be determined, which provides a compass to determine NV orientation, as discussed above. The NV spin sublevels are detected optically by the optically detected magnetic resonance (ODMR) technique [29]. Briefly the NV fluorescence strength depends on which spin sublevel is occupied so that spin transitions can be observed as dips in the fluorescence, even for single NVs.

Hollenberg et al. [98] demonstrated the ability to probe magnetic fluctuations in the local cellular environment

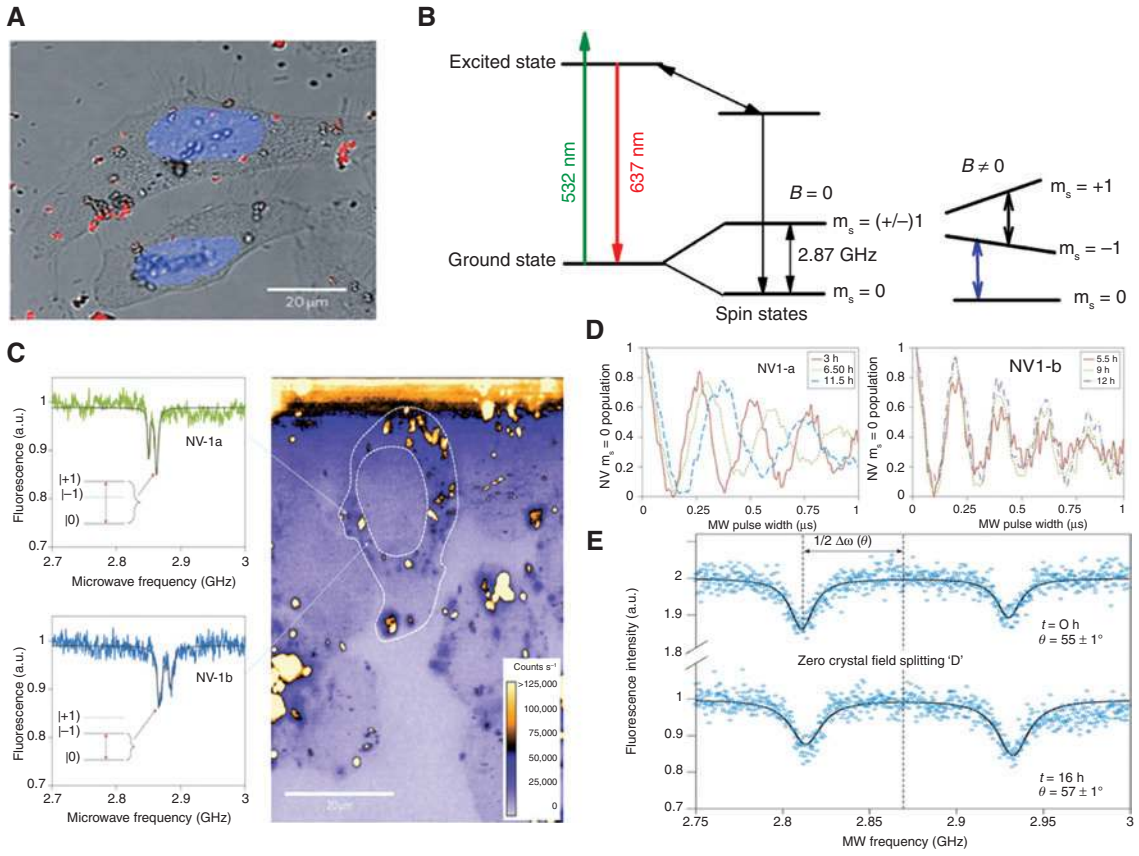

Figure 7: Tracking fluorescent nanodiamonds inside living cells process.
(A) Fluorescent nanodiamonds uptaken by HeLa cells. NV fluorescence is shown in red and the nucleus is stained with Hoechst 33342 (blue). (B) Electronic structure of NV color center in diamond. (C) ODMR spectra of NV-1a and NV-1b showing the different strain splitting between the two NV color centers. (D) Rabi oscillations of NV-1a and NV-1b measured at various times during the lifetime of the cell. (E) Changes in the orientation of the NV quantization axis relative to the external magnetic field owing to nanodiamond motion inside HeLa cell. Adapted from [98].

by measuring and monitoring the coherence time (T_2) of the NV probe [100, 101]. In particular, coherence times for both NV-1a and NV-1b color centers were measured by spin-echo techniques, and then repeated for each NV as the cell timeline progressed (over 10 h). Figure 7D shows coherent Rabi transitions of the NV center that are needed to produce the spin-echoes. They can be selectively excited by tuning a microwave (MW) field to the $|0> \rightarrow |+1>$ resonance for NV-1a or the $|0> \rightarrow |-1>$ resonance for NV-1b [98]. Finally, to track orientation of the individual NVs, they applied an external magnetic field and achieved an effective angular precision of 1° over integration times of 89 ms, as shown in Figure 7E [98].

3.1 Intraneuronal traffic readout with fluorescent nanodiamonds

A special case of intracellular tracking that takes full advantage of non-bleaching, non-toxic properties of NV nanodiamonds is the monitoring of intraneuronal traffic [102]. This work was motivated by the increase in human brain diseases around the world, which emphasizes a critical need for a comprehensive and detailed understanding of the extremely complex nature of the human neuronal system [103, 104]. Great efforts have been focused to mimic the abnormal cellular activities and physiological effects caused by neuronal diseases, largely by studying mice models [103–105]. Many of these studies used conventional fluorescent markers such as organic dyes, QDs, and fluorescent proteins for labeling neurons [106, 107].

Haziza et al. [102] studied intraneuronal transport by tracking FNDs in mouse hippocampal neurons, as shown in Figure 8A [102]. They imaged 30 nm fluorescent nanodiamonds inside the branches of dissociated neurons, as shown in Figure 8B, C [102] with a (subwavelength) spatial resolution of 12 nm and a temporal resolution of 50 ms. They then used these tracked particles as an assay to monitor the biological effects of certain chemicals (nocodazole) and genetic factors (*Mark1* mutants) that affect

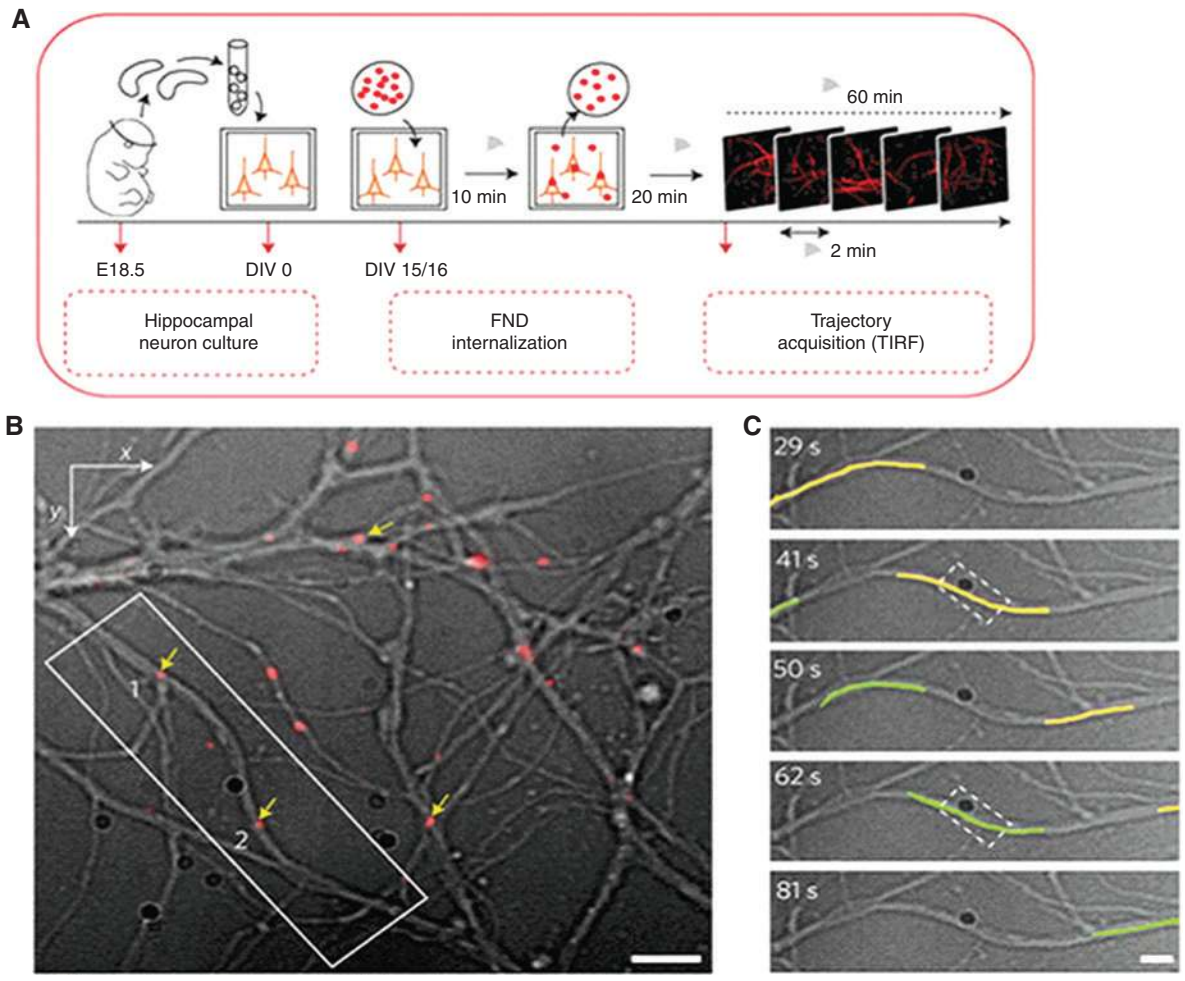

Figure 8: Intracellular tracking of fluorescent nanodiamonds in neuron.
(A) An experimental illustration from hippocampal neuron culturing and fluorescent nanodiamonds internalization to imaging. (B) Optical image of the neuronal branches merged with the fluorescence channel showing four FNDs moving within dendrites (yellow arrows). During the 2-min video, two FND-containing endosomes, labelled 1 and 2, were observed moving towards the cell soma in the same branch (scale bar, 5 μm). (C) Optical image of the positions of these two FNDs (1 in yellow; 2 in green), determined by particle tracking, with a persistence of 10 s, at different times. Adapted from [102].

intraneuronal transport dynamics [102]. Based on their success, they propose that combining FND technology with other state-of-the-art approaches, such as CRISPR/Cas9 genome editing [108] could lead to a deeper understanding of neuronal transport in normal, as well as disease states, including Alzheimer's disease.

4 Effects of rough nanodiamonds in living cells

So far, we have discussed some of the advantages of FNDs as excellent tools to study the complex processes of living cells [96–98]. However, the best FNDs, based on crushed HPHT nanodiamonds, typically have sharp edges, looking like broken panes of glass in the TEM [109]. This can have either good or bad effects on cellular imaging applications. The good effects are related to the lack of a general technique to efficiently internalize nanoparticles (NPs) into living cells. Many existing techniques are invasive and can have toxic effects on cells [110–112]. However, the rough edges of crushed FNDs can provide an alternative means of efficient delivery into living cells, as reported by Li et al. [113]. These authors found that FNDs with sharp shapes, regardless of their surface chemistry, size, or composition, entered the membranes of endosomes that carried them into the cells and escaped to the cytoplasm with high efficiency, as shown in Figure 9A [113]. This study further showed that a combined solution of prickly FNDs and SiO_2 NPs led to efficient internalization of the SiO_2 NPs, which otherwise would not have internalized,

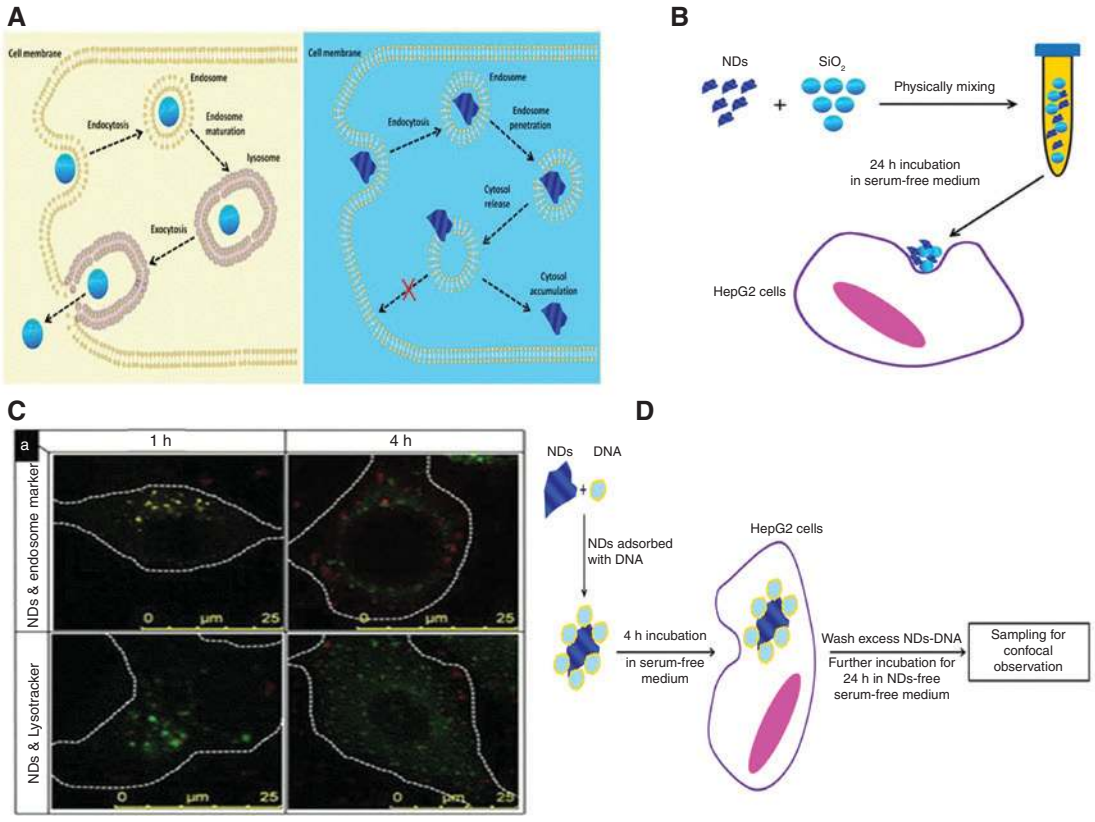

Figure 9: An illustration of rough nanodiamonds effects in living cells.
(A) An illustration showing nanoparticle (NPs) with low sharpness and sharp corners entering the cell. Left, round NPs enter cells via endocytosis with the endosome as the vehicle and finally exit the cell. Right: a sharp-shaped nanoparticle enters the cell via endocytosis with the endosome as the vehicle and escapes the endosome by rupturing the endosomal membrane and staying in the cytoplasm for a long time. Adapted from [113]. (B) A schematic demonstration of how nanodiamonds escape the endosomal membrane. (C) Confocal images of efficient nanodiamonds delivery into HepG2 cells after cell incubation with nanodiamonds in serum-free medium for 1 or 4 h. (D) A schematic illustration of nanodiamonds as a successful carrier for gene (DNA) in cells. Adapted from [114].

as shown in Figure 9B. They showed that the quick escape of NDs from the endosomes was realized by rupturing the endosomal membrane rather than slipping through it, as shown in Figure 9C [114]. They also demonstrated that prickly FNDs can be coated with DNA to effectively deliver it into cells. This led them to conclude that prickly FNDs make promising candidates for efficient drug delivery systems, as shown in Figure 9D.

5 Temperature sensing in living cells

Luminescence nano-thermometry has been demonstrated using QDs, organic dyes, gold nanoparticles (GNPs), and polymers to measure temperature changes in intracellular environments [115–118]. However, many of these fluorescent probes are limited by drawbacks including fluorescence fluctuations, such as photobleaching and blinking, particularly for dyes and QDs [116, 118], as well as fluorescence sensitivity to local environments [119]. The remarkable optical properties of nitrogen color centers (NV) in diamonds, which include photostability, spin long coherence time, and biocompatibility [96–98], make them one of the best alternatives for accurate temperature sensing.

Sensing temperature using the NV color center in diamond has been well-studied [120–122]. An increase in environmental temperature (T) can induce crystal expansion, which shifts the zero-field splitting of ground state toward smaller values as temperature is increased, as shown in Figure 10A [27]. These shifts were detected by ODMR [29], as will be discussed in more detail later in Section 6.2. The first application of fluorescent nanodiamonds (FNDs) as nano-thermometers in living organisms was done by Lukin et al. in 2013 [120]. They used 100 nm nitrogen-vacancy color center nanodiamonds to measure the local temperature of human living cells with a precision of 200 mK/$\sqrt{\text{Hz}}$ and a spatial resolution of 200 nm. Briefly, they injected laser-excited gold nanoparticles as a heat source (cross symbol) together with diamond

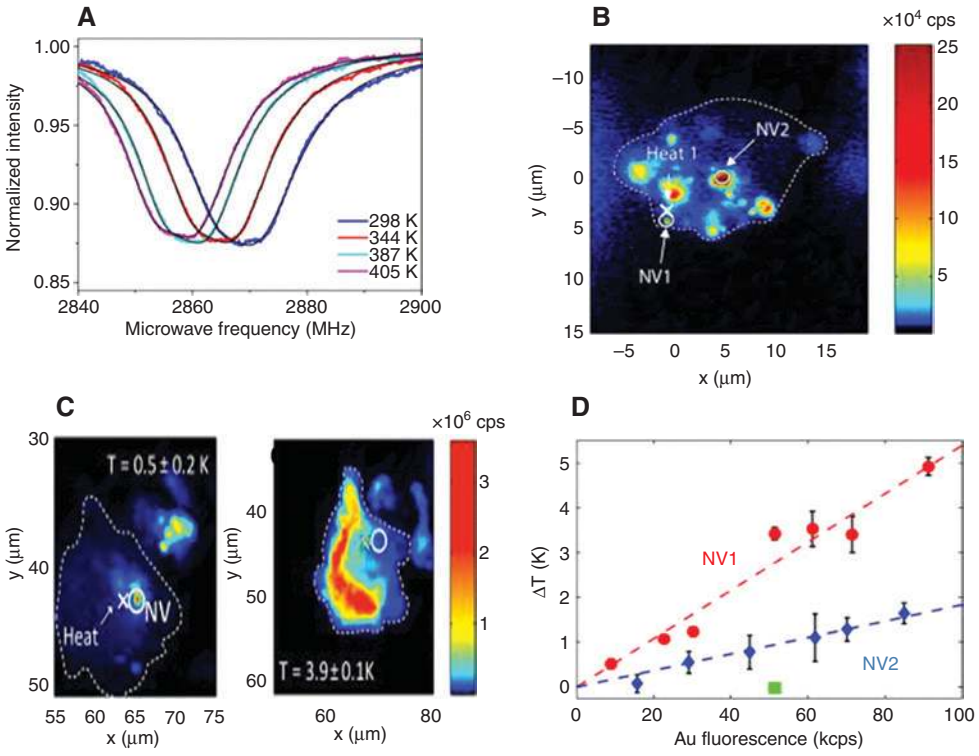

Figure 10: An optical temperature sensing application of FNDs (NV color center) in living cells.
(A) ODMR spectra of the NV color center change as a function of local temperature changes [27]. (B) A single living cell injected with fluorescent nanodiamonds and gold nanoparticles (Au NPs) as the heating source and nanoscale thermometer, respectively, followed by excitation under 532 nm. The position of the Au NP is indicated by small cross, while circles represent the location of the NV color centers in nanodiamonds used for thermometry. (C) Measurement of temperature changes precisely as the laser power increases with 0.1 K precision. (D) The change in temperature at the position of NV1 and NV2 relative to the incident laser power applied to the Au NP. Adapted from [120].

nanocrystals inside the living cells and used the NV center for thermometry (circle symbol), as illustrated in Figure 10B. They precisely measured the change in temperature at the position of NV1 and NV2 relative to the incident laser power applied to the Au NPs, as shown in Figure 10C, D [120].

Following this, there were several other notable achievements in the field of the NV-based nanoscale temperature sensing in biological applications [121, 123, 124]. Remarkably, Wang and his co-authors [125] reported that the temperature sensitivity of the NV center in nanodiamonds can be increased by two orders of magnitude beyond the sensitivity reported in [120]. This was done using a hybrid nano-thermometer composed of NV centers and a magnetic nanoparticle (MNP), in which the temperature sensitivity is enhanced by the critical magnetization of the MNP near the ferromagnetic-paramagnetic transition temperature.

In addition to NV, almost all narrowband emitters in diamond have temperature dependence and can be used as a nano-thermometer without the need for microwaves. For example, nano-thermometry with SiV [126] and GeV [127] has been explored recently, where in the case of SiV the excitation and emission is in the tissue transparency window.

Here, it is important to note that there has been some recent controversy in the field of cellular temperature measurement. Specifically, it was argued that the temperature changes reported by many experiments could not have been possible based on simple thermodynamic arguments [128], and hence, there must have been unknown interferents present in the cells that led to false temperature readings. To address this controversy multi-modal temperature measurement is a good approach, in which two or more temperature probes simultaneously measure temperature. Provided these probes sense temperature by different physical mechanisms, they will not respond to interferents in the same way, and therefore false readings can be ruled out [109].

5.1 Temperature sensing in neurons

The temperature sensing capability of fluorescent nanodiamonds, together with their low toxicity suggests possible uses in the treatment of nervous system-related diseases

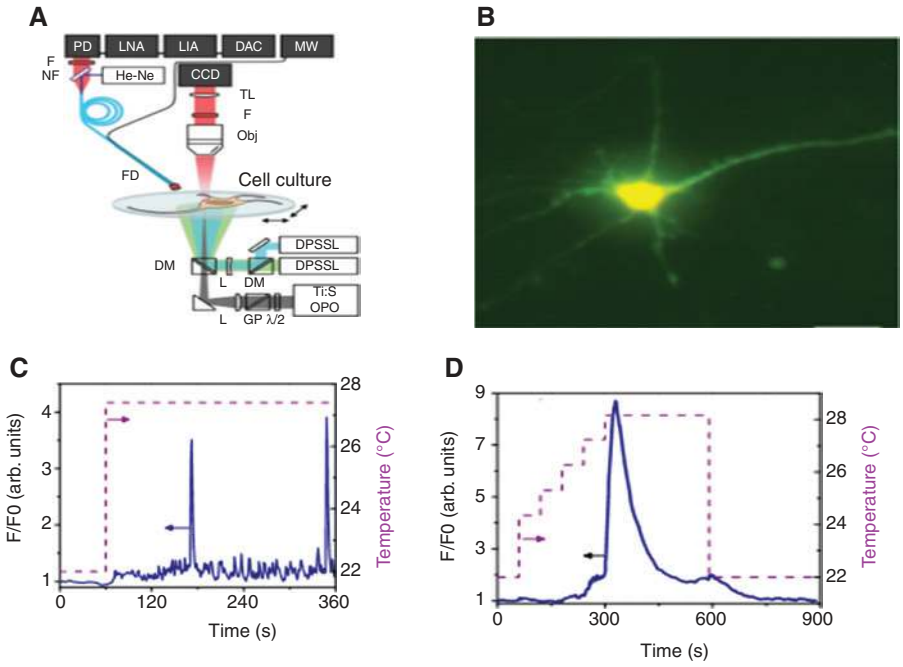

Figure 11: Temperature sensing capability of FNDs (NV center) in neurons.
(A) An illustration of experimental setup of fiber-optic thermometry of single thermogenetically activated neurons, details about the system in [132]. (B) Fluorescence image of a laser-activated neuron. Fluorescence of the Ca^{+2} sensor in a laser-activated neuron (solid line) increases (C) or decreases (D) as the temperature increases or decreases (dashed line) above or below the activation threshold for TRPA1-expressing neurons. Adapted from [132].

and injuries. For example, monitoring the thermal state of the nervous system is very important to determine the effects of temperature on its operation. As a special case, consider neurons that sense warm, cold, and hot conditions, which have specialized ion channels that convert heat into action potentials [129–131]. Zheltikov and his co-workers have demonstrated the ability to accurately measure the local temperature of TRP-expressing mouse neurons using fiber-coupled NV centers in micron-size diamonds [132], as shown in Figure 11A [132]. Here the mouse neuron was labeled with GCaMP6s fluorescence to serve as a calcium sensor, as shown in Figure 11B [132]. This calcium sensor detects neuron firing via the inward Ca^{2+} current across the cell membrane. When the temperature reaches the neuron activation threshold ($T_a = 27.4°C$), neurons expressing transient receptor potential (TRP) action channels [132] begin to fire, producing spikes of GCaMP6s fluorescence, as shown in Figure 11C [132]. On the other hand, when the temperature decreases below the activation threshold, the fluorescence of the Ca^{+2} sensor in the neurons gradually decreases, as shown in Figure 11D [132]. The temperature reading of single neurons obtained with the NV-diamond fiber sensor strongly correlates with the fluorescence of the calcium-ion sensors. This study opens the door for eventually using fiber-mounted FNDs for temperature sensing in live brains.

6 Other capabilities of fluorescent nanodiamonds

6.1 Super-resolution with fluorescent nanodiamonds

Fluorescence microscopy is an enormously powerful technique to study complicated biological structures down to the sub-cellular level in biological applications [133]. However, the diffraction limit of light is an obstacle that prevents detailed visualization of subcellular processes. In the past couple of decades, super-resolution imaging microscopy has overcome the diffraction limit of light. There are two main approaches: PALM/STORM and variants that rely on controlled bleaching and measurement of centroids, and stimulated emission depletion (STED)/ground state depletion (GSD), which rely on the use of donut beams. STED microscopy works when two laser beams at different wavelengths are superimposed. The first (main) laser beam excites the fluorescent marker of interest to its excited state. The second laser beam with a doughnut shape at its focus depletes the fluorescence from all molecules except those in the middle of the excitation volume. Consequently, the resultant "fluorescent volume" becomes smaller than the diffraction limit [27, 134], as shown in

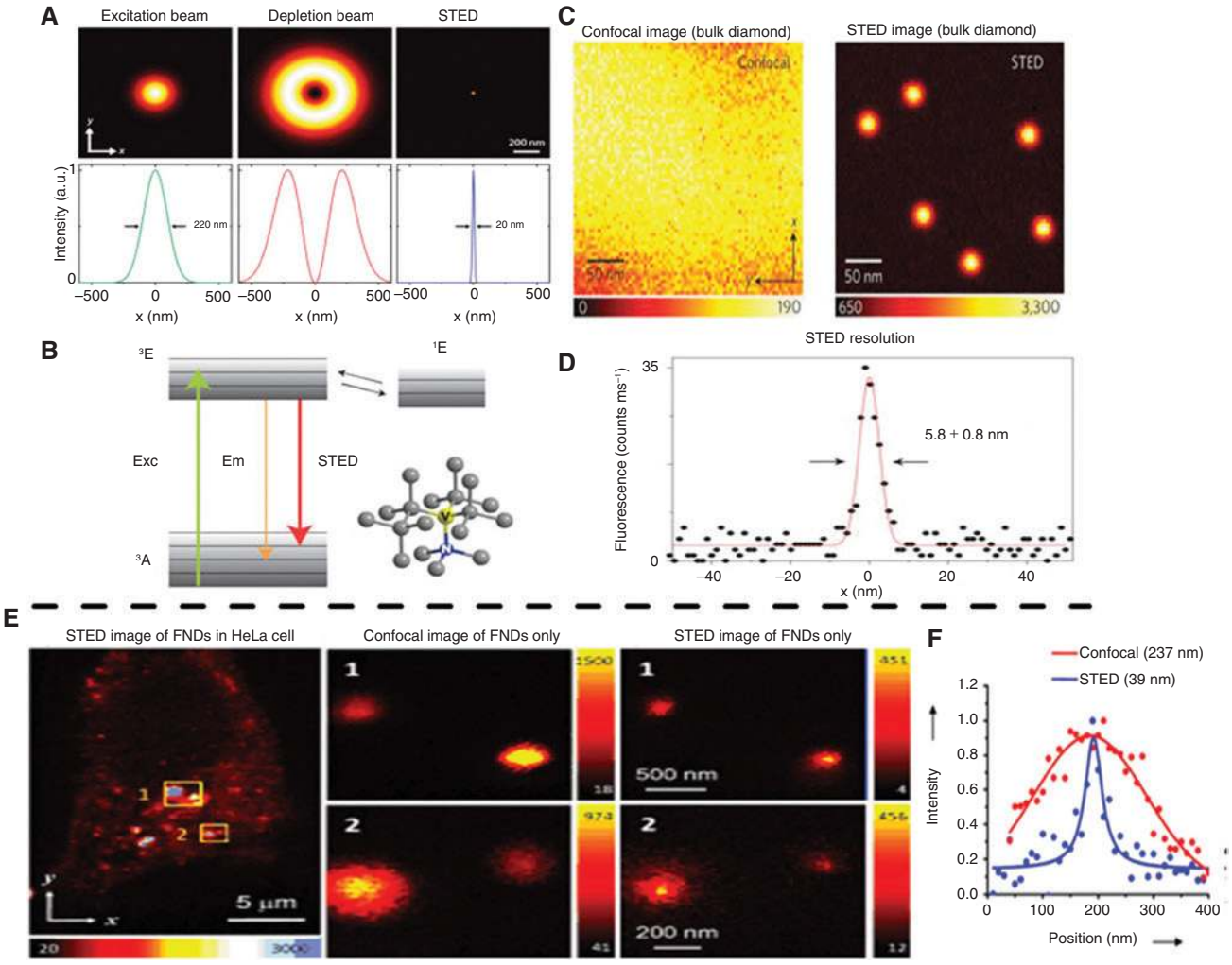

Figure 12: Applications of FNDs (NV center) in super-resolution imaging.
(A) An illustration of STED microscopy technique. Adapted from [134]. (B) Energy levels of the triplet (left) and singlet states (right) of the NV center and the excitation beam (EXC), emission beam (Em), and stimulated emission (STED) transitions in nitrogen-vacancy centers. (C) Confocal and STED optical image of bulk diamond containing NV color centers. (D) STED high resolution for NV center in diamond, which reveals high spatial resolution reaching 5.8 ± 0.8 nm. Adapted from [135, 136]. (E) Confocal and STED imaging of HeLa cells labeled with BSA-conjugated FNDs through electroporation. STED images of single BSA-conjugated FND particles enclosed within the yellow boxes "1" and "2". (F) Display of confocal and STED resolution of NV centers within diamond nanocrystals. Adapted from [137].

Figure 12A [134]. Hell and co-workers used diamond color centers in STED field and achieved a remarkable resolution of ~6 nm by detecting single NV centers in bulk diamonds, as shown in Figure 12B–D [135, 136].

The reason the nitrogen-vacancy color center in diamond gives such high spatial resolution with STED is due to its long-term photostability, even for very strong excitation intensities. For STED with nanodiamonds, a study by Tzeng et al. [137] obtained a resolution of ~40 nm of fluorescent nanodiamonds in HeLa cell, as shown in Figure 12E, F. A later study by Hell and his co-workers [138] has also shown that individual NVs within single nanodiamonds can be resolved with 10 nm resolution, which is even smaller than the size of the nanodiamond (average size 40–250 nm). This study highlights the need for smaller nanodiamonds with stable color centers.

6.2 Sensing magnetic field, electric field, and temperature

Color centers in diamonds, especially the NV color center, have considerable potential in quantum limited sensing of important physical quantities, such as magnetic fields [139], electric fields [140], and temperature [141]. For magnetic field sensing, a single NV center in an ultra-pure bulk diamond can detect magnetic fields with sensitivity of a few $nT/\sqrt{\text{Hz}}$ [142, 143]. In principle, this has

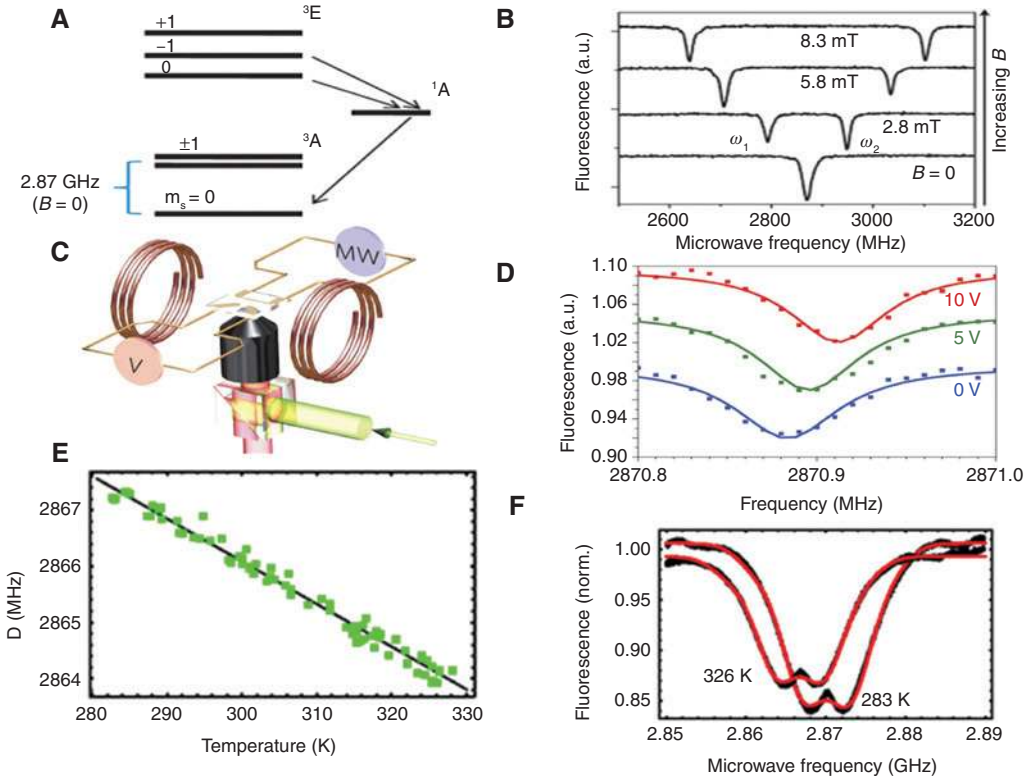

Figure 13: An illustration of FNDs capability in magnetic, electric, and temperature sensing.
(A) An illustration of the energy level of the nitrogen-vacancy (NV) defect in diamond. (B) Optically detected magnetic resonance spectra (ODMR) for a single nitrogen-vacancy defect at increasing magnetic field (from bottom to top). Adapted from [144]. (C) Schematic of the confocal set-up used with Helmholtz coils for magnetic field alignment and a microstructure on the diamond sample to create the electric field and coupled with the microwaves. Adapted from [140]. (D) Observed shift of the ODMR resonance lines for different voltages applied to the electrodes, clearly showing the effect of a Stark shift. Adapted from [140]. (E) A linear fit of the NV center ODMR spectra changes as a function of ambient temperatures. Adapted from [146]. (F) ODMR changes linearly as a function of temperatures from 280 to 330 K. Adapted from [146].

nanometric spatial resolution owing to the small size of the NV [144]. For biological applications, magnetic field detection has been proposed to non-invasively monitor neuron firing [100, 145], and electric fields to monitor membrane potentials [29].

The NV color center senses magnetic fields via the ODMR [29]. Briefly, the NV has an $S=1$ spin ground state, which is split into three spin sublevels ($m_s=\pm1$ and $m_s=0$) with zero-field splitting $D=2.87$ GHz due to spin-orbit interactions and the diamond crystal field, as shown in Figure 13A [99, 144]. The optical pumping excitation polarizes the NV center into the $m_s=0$ spin sublevel via intersystem crossing to an intermediate singlet state. This crossing occurs only for spins in the $m_s=\pm1$ states, which then decay into the $m_s=0$ state. Since the intermediate singlet is dark and has a relatively long lifetime, NV spins in the state $m_s=0$ fluoresce brighter, emitting ~30% more red photons than NVs in the $/m_s=\pm1$ states. Hence, when a resonant microwave field induces magnetic dipole transitions between these spin sublevels, it equalizes the spin populations, resulting in a significant decrease of the nitrogen-vacancy center fluorescence [144]. Due to symmetry, the $m_s=\pm1$ sublevels of the nitrogen-vacancy defect are degenerate at zero magnetic field ($B=0$), resulting in a single resonance line appearing in the ODMR spectrum, as shown in Figure 13B. An external magnetic field lifts the degeneracy of $m_s=\pm1$, leading to the appearance of two lines. The external magnetic field can be measured from the positions of these two lines (w_1 and w_2), as shown in Figure 13B. The separation between the ODMR two lines increases as the axial magnetic field increases [144], and in addition both lines can shift in the same direction for non-axial magnetic fields.

For electric field sensing, Wrachtrup and his co-workers have demonstrated electric-field sensitivity reaching 202 ± 6 V/cm/Hz$^{1/2}$ using the NV color center in bulk diamonds [140]. The electric field was generated by the application of a controlled voltage to a gold microstructure fabricated by lithography and electroplating directly on a bulk diamond sample containing NV centers, as shown in

Figure 13C [140]. To measure electric-field-induced shifts of spin sub-levels, they monitored the zero-field splitting of the $m_s = 0$ and $m_s = \pm 1$ transition, which is split by the local crystal field. They observed a resonance line shift (or increase in the zero field splitting) of 28.4 kHz corresponding to an electric field of about 3000 V/cm. Figure 13D shows the shift of the ODMR resonance frequency for different voltages applied to the electrodes [140].

As previously mentioned, M. Lukin and co-workers used the NV for temperature sensing at precision up to 1.8 mK/$\sqrt{\text{Hz}}$ in ultra-pure bulk diamond [120]. However, in living cells, the precision was only 200 mK/$\sqrt{\text{Hz}}$ due to the relatively worse spin line width in nanodiamonds [120]. As discussed earlier, the mechanism of temperature measurement is the shift of the zero field splitting, which is near $D = 2\pi \times 2.87$ GHz at room temperature, as shown in Figure 13E, F [146, 147].

6.3 Single protein detection via magnetic relaxation

Several years ago, it was proposed to use NV centers to detect and resolve the structure of single biological molecules (like proteins) through dipolar coupling to the nuclear spins of the protein [148–150]. In the case when the biomolecules have rapidly fluctuating spins, the NV can easily detect their presence via its accelerated magnetic relaxation. This was recently accomplished by Jelezko and co-workers who detected ferritin molecules on the surface of nanodiamonds by observing a significant reduction of both initial coherence and relaxation time of the NV color center in FNDs [151]. They attached ferritin molecule to the surface of fluorescent nanodiamonds by noncovalent binding to the amino groups of the protein. The nanodiamond–ferritin complexes were first visualized by high-resolution

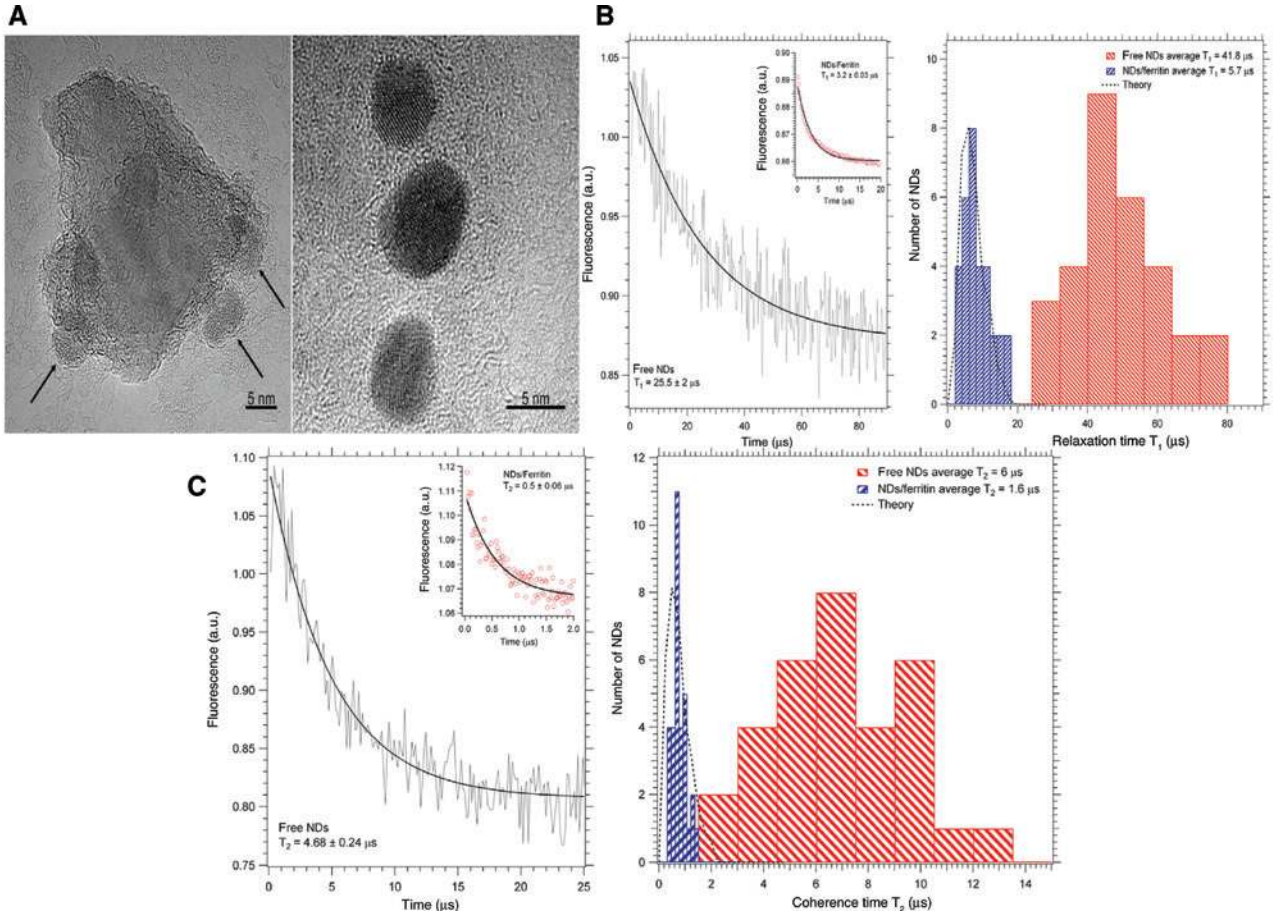

Figure 14: Single protien detection via magnetic relaxation of the NV center in FNDs.
(A) High resolution images of ferritin molecules (right) showing the iron containing core and single nanodiamond covered with ferritin (left). The arrows indicate the position of the metalloprotein on the surface of the NDs. (B) The electron spin – lattice relaxation time T_1 of NV in NDs without coating with protein (left) and in ferritin coated NDs (left, inset). Statistical distribution of the T_1 for free nanodiamonds (right, blue bars) and for ferritin coated nanodiamonds (right, red bars). (C) The electron spin – lattice relaxation time T_2 of NV in NDs without coating with protein (left) and in ferritin coated NDs (left, inset). Statistical distribution of the T_2 for free nanodiamonds (right, blue bars) and for ferritin coated nanodiamonds (right, red bars). Adapted from [151].

transmission electron microscopy (HRTEM), as shown in Figure 14A [151]. At room temperature, the iron electron spins in the protein molecule undergo rapid thermal fluctuations, which create a strongly fluctuating spin bath. This bath couples to the electron spin of the NV, shortening both the spin coherence time T_2 and the spin population relaxation time T_1 by an order of magnitude when compared to non-coated nanodiamonds, as shown in Figure 14B, C [151]. As an indication of the ultimate sensitivity of this technique, we note that single Gd ions were detected by similar techniques [152].

6.4 Single protein imaging in live cells

One especially ambitious potential application of NV diamond is to image single protein molecules in live cells [153]. Initially, magnetic resonance force microscopy (MRFM) [154] was developed for this purpose, and successfully imaged single electrons and tobacco virus particles [154], but required cryogenic temperatures, and was therefore not suitable for live cells. In recent years, attempts have been made to use the NV for this purpose owing to its nanoscale magnetic sensing capability. The basic idea is to use the NV to measure magnetic fields produced by nuclei in the protein molecule. Then, by selectively driving individual nuclei in the protein using magnetic resonance imaging (MRI) techniques, an image can be constructed in principle [155].

The first successful detection/1D imaging of a near-single electron spin was done by [156] using a technique called double electron-electron resonance [156, 157]. Here, the magnetic gradient needed for 1D imaging was supplied by the field of the NV itself, which decayed as $1/r^3$ (r is distance of the electron from the NV). Later, this technique was applied to imaging of a few silicon nuclei [158] and ensembles of nuclei near single NVs in bulk diamond. Finally, the technique was extended to detect single nuclei outside the diamond via dark "reporter" spins on the diamond surface [159] or spin labels attached to a position of interest on the protein [155]. To successfully transition this single protein imaging technique to live cells, ultrasmall nanodiamonds with stable NVs that have spin sensitivities comparable to bulk diamond are required.

7 Hyper polarization with NDs

Magnetic resonance imaging (MRI) is a powerful technique for high-contrast imaging, but it requires large DC magnetic fields to achieve good nuclear spin polarization at room temperatures. This is because of the small nuclear spin flip energy compared to the Boltzmann energy, kT. Electron spins, in contrast, have much larger polarization owing to their larger electron spin flip energy. By using the Overhauser effect [160], it is possible to transfer this electron polarization to the nuclear spins [161]. While many paramagnetic particles have been explored for this purpose [162–165], NDs have the advantage of excellent biocompatibility and chemical stability.

Recently, Waddington et al. [166] demonstrated a Overhauser-enhanced MRI (OMRI) technique [166–170] to image and track water–ND solutions. This is done by transferring the electron spin polarization of paramagnetic impurities at the surface of NDs to ^{1}H nuclei continually in the surrounding water [171]. To maximize the nuclear polarization efficiency, they use ultra-low magnetic fields (ULF; 6.5 mT) and low frequency RF (~190 MHz) excitation, which have the advantage of being compatible with *in vivo* use. The result was switchable contrast enhancement at biologically relevant ND concentrations. In particular for this experiment, they focused on HPHT NDs with sizes of 18 and 125 nm in DI water at concentrations near 100 mg/ml [166].

The mechanism of the Overhauser effect from ND surface spin impurities to water is illustrated in Figure 15A [166]. Briefly, Overhauser effect occurs when a reservoir of polarized electron spins on the NDs' surfaces are driven by a resonant RF magnetic field at low enough DC magnetic fields that mutual electron-^{1}H nuclear spin flips can occur in the surrounding solution [172, 173]. This results in enhanced ^{1}H signal from the water surrounding the ND, as shown in Figure 15B [166]. The ^{1}H signal enhancement is sensitive to ND concentration, as illustrated in Figure 15C [166]. After optimizing the experiment conditions to achieve high contrast OMRI images enhanced with NDs, a phantom is imaged, as illustrated in Figure 15D [166]. This phantom consisted of glass vials filled with 500 µl of either pure DI water or aqueous solutions of HPHT ND (125 nm at 100 mg/ml). A high contrast OMRI image of diamond-shaped pattern in the vials was observed, as shown in Figure 15E [166], which shows high-contrast signal enhancement only where ND is present. Furthermore, they demonstrated that the OMRI technique can produce gray-level images using different ND concentrations, as shown in Figure 15F, G [166].

Much stronger MRI contrast enhancement is possible in principle using NVs that are strongly spin polarized (up to 90%) [174] by optical excitation. This polarization can then be transferred to nearby nuclear spins like ^{13}C or ^{1}H [174, 175]. Recently, it has been shown that the ^{13}C in bulk diamond can be polarized to 0.054% at room temperature (45-fold enhancement) after 6 min of optical excitation of the NVs at a magnetic field of ~0.3 T [174]. However, it has also been reported [174, 175] that the relaxation time of

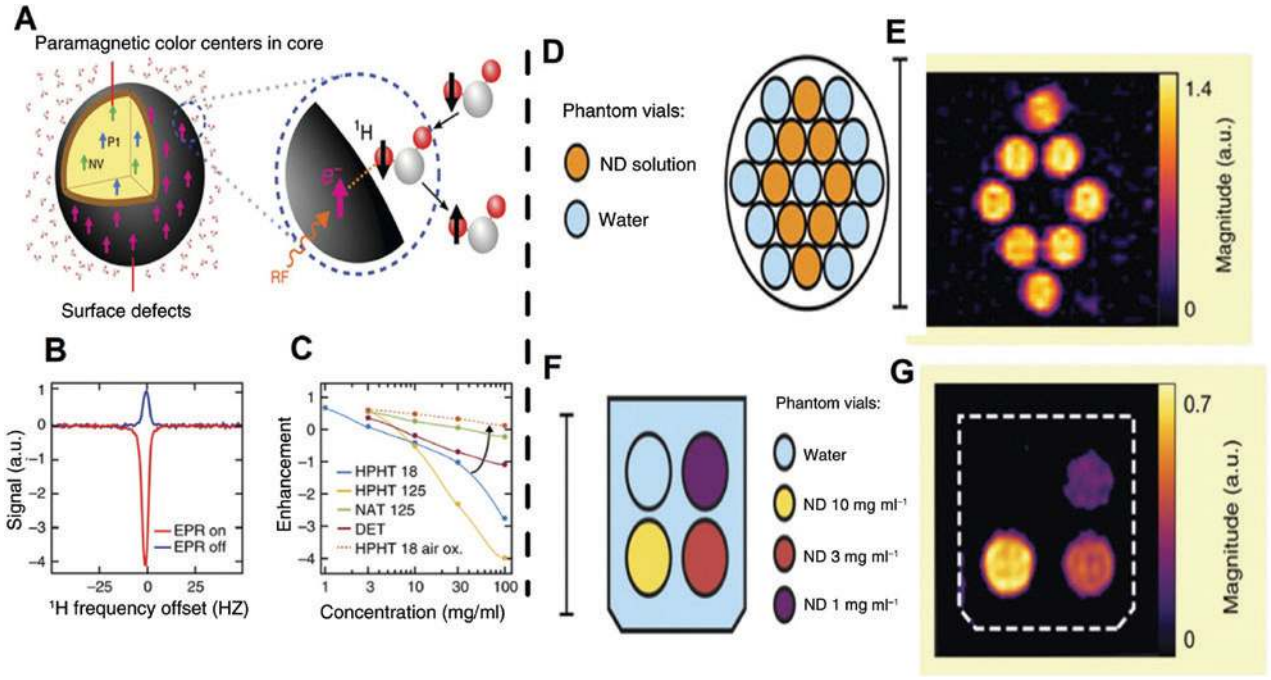

Figure 15: Hyper-polorization applications of nanodiamonds.
(A) An illustration of the Overhauser effect at the ND–water interface. (B) Overhauser enhancement of ^{1}H polarization in an HPHT 125 nm (100 mg/ml) ND solution (red). While the thermal hyperpolarized ^{1}H spectrum is (blue). (C) Overhauser enhancement of ^{1}H polarization as a function of NDs concentration at 6 mT. (D) Vials of DI water (blue) and vials of HPHT 125 nm ND at 100 mg/ml (orange) were arranged in a pattern in an imaging phantom. (E) High contrast OMRI image with high signal to noise ratio from only the vials where NDs are present. (F) Imaging phantom prepared with vials with different concentration of ND solutions. (G) ODMR contrast images that change as a function of the NDs concentrations. Adapted from [166].

hyperpolarized nuclei is much shorter for submicron particles [163, 166, 176]. Nonetheless, it has been shown that high contrast MRI images can be produced from spin polarized ^{13}C owing to the lack of background ^{13}C signals [177]. Finally, at cryogenic temperatures, dynamic nuclear polarization (DNP) of the ^{13}C nuclei can boost the small nuclear spin polarization by 10,000 times [176, 178, 179]. However, these temperatures are not suitable for *in vivo* work.

Efforts have been made to overcome the short relaxation time of nanodiamonds at room temperature by functionalizing the surface of the DNDs with paramagnetic Gd(III) chelates to create complexes for imaging with conventional T1-weighted MRI [164]. However, this alternative solution encountered a large background signal and concerns of the long-term toxicity of gadolinium-based compounds cancel the advantage of non-toxic nanodiamonds [165].

8 Nanodiamonds in high contrast molecular imaging

Molecular imaging is a powerful technique to image biochemical differences in living organisms [180]. Molecular imaging can be done both on the cellular and tissue level. For example, contrast agents for tissues include those that can be detected by magnetic resonance imaging, X-ray tomography, and optical fluorescence. However, deep in the tissues, existing techniques tend to lack either sensitivity or spatial resolution [180–183].

One way to overcome these limitations is to use diamonds containing nitrogen-vacancy color centers. Briefly, because NVs show a magnetic sensitivity that reaches a few tesla ($nT/\sqrt{\text{Hz}}$) in pure bulk diamonds [184], it should be possible to achieve high spatial resolution by applying magnetic field gradients to tissues containing NVs. The position of the nanodiamonds can then be determined by using ODMR. It has been shown that nanodiamonds having NV-centers can achieve magnetic sensitivity of 10–20 μT. For a 1 T/m, this would give a spatial resolution of ~20 microns [185, 186].

Recently, Hegyi et al. demonstrated NV-based molecular imaging approach using magnetic gradients of ~1 T/m. They started with FNDs and showed a sensitivity as low as 100 fg with spatial resolution reaching 100 μm [187]. For tissue samples, they later used chicken breasts (1 cm×1 cm×2 cm) with FNDs implanted, as shown in Figure 16. Different shapes of FND phantoms were made out of a double-stick tape (1 mm×1 mm) covered with a 3.75-μg-mm^{-2} area density of NV FNDs, which was then

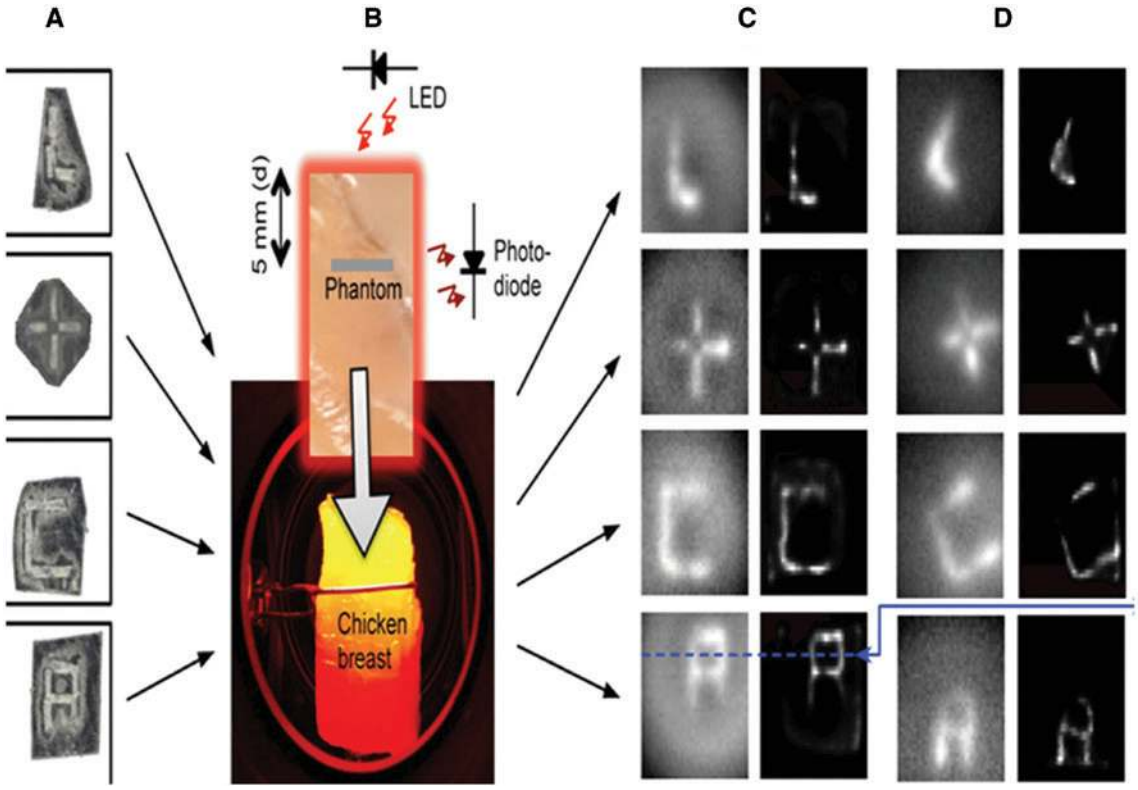

Figure 16: Nanodiamonds in high contrast molecular imaging.
(A) Nanodiamond phantoms (with different patterns) made of double-sticky tape. (B) The gray stripe on the piece of chicken breast represents the edge of the phantom, which is placed inside the chicken breast, 5 mm back from the front surface, facing the LED. Fluorescence is collected off to the side. Also shown is the actual piece of chicken breast illuminated by the LED. (C) The phantoms imaged outside of the chicken breast, both before (left) and after (right) deconvolution by the point-spread function. (D) Same as (C) but under a 5-mm chicken breast. Adapted from [187].

positioned inside the tissue, at a depth of 5 mm, as shown in Figure 16A, B.

The nitrogen-vacancy centers were optically excited by a red LED at wavelength 610–630 nm placed near the tissue. Relatively low optical intensity of ~1 W/cm^2 was used to illuminate the chicken breast. The achieved sensitivity and the spatial resolution in chicken breast tissue were, respectively, 740 pg of ND with 800 µm resolution over a 1-cm^2 field of view, after 100 s of averaging time. To produce images, they used four permanent magnets to generate a field-free point, plus electromagnets to scan the position of this point through the tissue in real time. For 2D images, a raster scan pattern was applied. For 3D images, rotated 2D projections and field-free lines, instead of points, were used instead to shorten acquisition time. A single point detector was used to measure changes in the photoluminescence. To maximize the resolution, they first measured the point spread function (PSF) and deconvolved it to produce the final images, as presented in Figure 16C, D. From this data, they conclude that nanodiamonds imaging may become an important biomedical research tool with possible clinical applications.

Recently, Singam and his co-authors demonstrated high-contrast imaging by using strong laser excitation to enhance the magnetic sensitivity of FNDs containing NVs. Surprisingly, they found that static magnetic fields (SMF) perform better than the usual resonant microwave field (RMF) excitation under strong laser excitation. This is an advantage because microwaves can have unwanted heating effects. They demonstrated the ability of this high magnetic contrast to effectively suppress background bio-fluorescence from neurons loaded with FNDs [188]. In principle, this stronger magnetic contrast can also be used to enhance the performance of molecular imaging in tissues, as described above.

9 Diamond Raman and fluorescence for environmental bacteria detection

In addition to fluorescent color centers, diamond has a bright and distinct narrowband Raman line at 1332 cm^{-1}

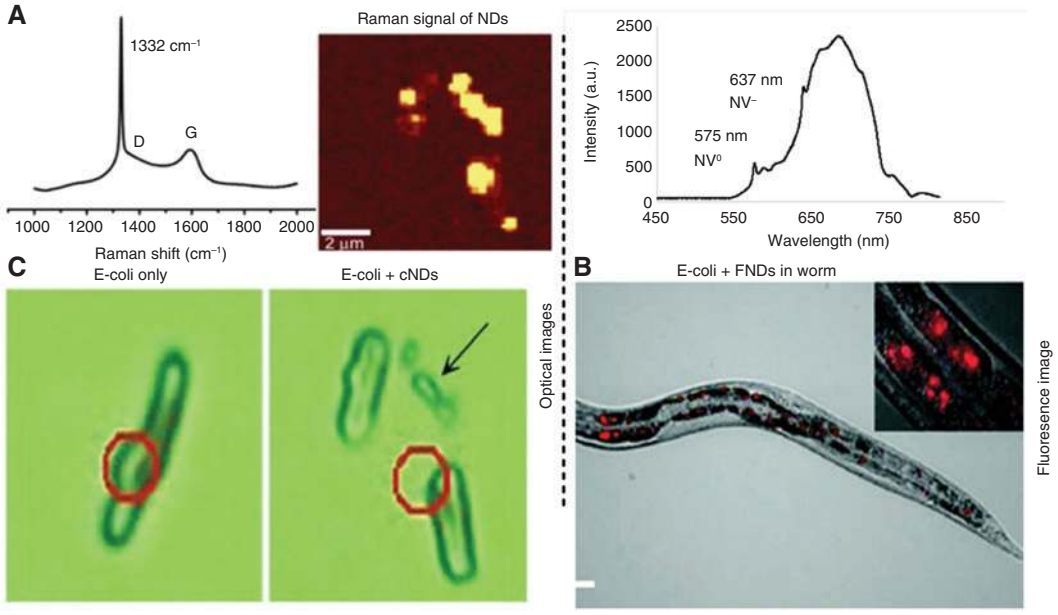

Figure 17: Diamond optical Raman and fluorescence signals for bacteria detection.
(A) Raman peak of 100 nm diamond peaks at 1332 cm^{-1} (left). Optical Raman signal of NDs during the interaction of *E. coli* with cND-lysozyme complex (right). (B) NV center fluorescence of 100 nm interacted with *E. coli* inside a worm. Red spots are the NV luminescence in the optical image. (C) In the optical images, *E. coli* cells can be seen but the NDs cannot be seen beyond the diffraction limit of optical microscopes. Adapted from [47, 195].

that can be used to detect its presence. The advantage to Raman is that the Stokes shift is independent of excitation wavelength, so it can be excited by near infrared light in the tissue transparency window where autofluorescence is suppressed. The disadvantage is that the quantum efficiency is low so that a larger quantity of nanodiamonds is needed to produce a clear signal. By functionalizing nanodiamonds (NDs) to stick to specific bacteria, this Raman line, as well as fluorescent diamond color centers, can be used for bacteria detection. There is a need for selective detection of specific bacteria because not all bacteria are pathogenic and not all pathogenic bacteria infect humans. However, mortality caused by bacteria-induced illnesses, such as tuberculosis, whooping cough, and typhoid fever, are a significant global concern. Thus, there is a need to develop simple, large-scale, and rapid methods to detect bacterial pathogens in blood, sputum, urine, stools, as well as our food and water supplies.

As an example, consider *Escherichia coli* (*E. coli*) which is a Gram-negative bacterium commonly found in intestines. Some strains of *E. coli* are known to cause disease, including pneumonia, urinary tract infections, and diarrhea. This has motivated numerous efforts to come up with easy and rapid detection methods [189]. Commonly, researchers use fluorescent proteins (e.g. green fluorescent protein and luciferase) as reporters [190, 191]. However, they have two major disadvantages: low signal-to-noise ratio due to autofluorescence of clinical samples and bacterial cells, and low photostability (photobleaching) [192, 193]. Quantum dots have been used for pathogen detection [194], but their cytotoxicity is a limitation.

Fluorescent (or Raman active) nanodiamonds are an alternative for *E. coli* detection owing to their great photostability and extraordinary biocompatibility [96–98]. As already mentioned, the surface of FNDs can be easily modified chemically [53] and conjugated with proteins, such as lysozyme, through physical adsorption [195]. Such FND-protein bioconjugates allow visualization of the protein-bacteria interaction either via the detection of the diamond Raman signal, as shown in Figure 17A, or for a low concentration of target bacteria, by detection of fluorescence color centers, as shown in Figure 17B, C [47]. In both cases, the function of the test protein is preserved [195].

10 Fluorescent nanodiamond-bacteriophage conjugates

Bacteriophages (phages for short) are simple viruses that infect specific bacteria as their hosts [196]. They are of much recent interest as potential replacement for antibodies because they are highly selective, attacking only

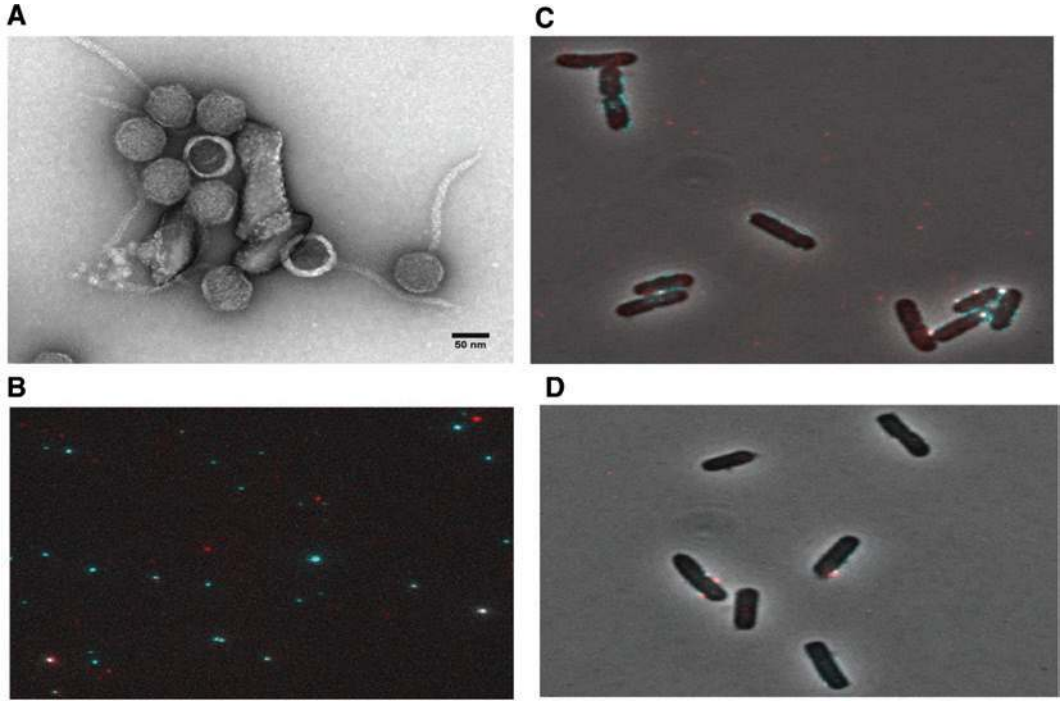

Figure 18: Fluorescent nanodiamonds-bacteriophage conjugates maintain host identification.
(A) High magnification TEM images of biotinylated bacteria phages bound to streptavidin-functionalized FNDs. (B) Optical image of biotinylated bacteria phages (blue spots) bound to streptavidin-functionalized FNDs (red spots). (C and D) Optical images of biotinylated bacteria phages (blue spots) bound to streptavidin-functionalized FNDs (red spots) that have infected bacterial cells (*E. coli*).

one type of bacteria at a time. Phages have a rich research history spanning over six decades since its discovery [196]. Phage lambda (λ), explored in our recent work, targets *E. coli* [197, 198]. Currently, conventional fluorescent markers (e.g. GFP and luciferase) are used to visualize the phage, as it attaches to its host during infection [190, 191]. However, these dyes have two major disadvantages: low signal-to-noise ratio due to autofluorescence of clinical samples and bacterial cells, and low photostability (photobleaching) [193, 194]. As an alternative, quantum dots were proposed [192, 194], but their possible toxicity is an issue. Therefore, we investigated fluorescent nanodiamonds as markers for phages [199–201].

Our goal was to modify the exterior of the phage to accept fluorescent diamond nanoparticles in order to visualize the phage as it is attached to its host during infection. To this end, we have successfully engineered biotinylated head protein of the phage and bound them to streptavidin-conjugated nanodiamonds, as shown in Figure 18A, B. We also tested the ability of the phages-FNDs complex to infect *E. coli*, as shown in Figure 18C, D [202]. This illustrates the application of tagged phages as selective bacteria detectors. Clearly, to reach our goal of imaging the phage infection process, we need much brighter and smaller nanodiamonds.

11 New color centers in diamonds

The NV center is the most extensively studied type of fluorescent diamond and expectations of its potential use in biological and biomedical applications have been high. However, NV centers have certain limitations which need to be appreciated. The first is the well-known reduction of brightness of NV centers as nanodiamond size falls below 50 nm and approaches the single-digit regime [203]. This is relevant for applications such as bioimaging where small size is essential for *in vivo* imaging. On a related note, although NV center nanodiamonds emit fluorescence in the NIR, which is desirable for *in vivo* imaging, they are often excited with green light lasers, which does not penetrate tissues very well. However, there are several recent examples of NV nanodiamonds that give bright fluorescence even with red laser excitation (~630 nm or longer) [132, 187].

Another point to recognize about NV-center fluorescence is that it is very broad (between 630 and 800 nm) [29]. This poses a problem as it significantly limits multiplexing with other fluorescent probes. Multiplexing is a common and powerful method used in many biological applications in which multiple fluorescent probes with non-overlapping emission are used to generate data for

multiple markers simultaneously. Multiplexing is especially important for markers, which may only be available in small amounts (e.g. tumor tissue from a patient). For example, it would not be possible to multiplex using an NV center as a fluorescent probe, along with a far red fluorescent protein [204, 205] and/or antibodies labeled with Alexa Fluor 750, since the broad fluorescence of the NV center would bleed into both of the channels used to detect the other fluorescent probes.

Thus, while there are numerous applications for NV-center diamonds, there is also a need for other "next-generation" fluorescent nanodiamonds that possess features not available with NV centers. One desirable feature is to have bright fluorescent nanodiamonds with sizes below 10 nm. The brightness would need to be observable using conventional bioimaging equipment, (e.g. LiCor Pearl or Odyssey systems or Perkin Elmer IVIS system). Typically, commercial instruments are less sensitive than the custom-built fluorescence systems found in many academic laboratories. Another desirable feature would be to have color centers that can be excited within the NIR window and emit fluorescence further out in the NIR. This would overcome the poor penetration of excitation wavelengths in the visible region and allow fairly deep tissue penetration *in vivo*. Finally, a third desirable feature would be nanodiamonds that possess sharp, narrow emission peaks, which could allow multiplexing with other fluorescent probes. In the following sections, we describe a collection of such "next-generation" fluorescent nanodiamonds that have recently been investigated which meet these expectations.

Fluorescent nanodiamonds that have absorption and emission bands located within the biological transparency window are of particular interest for biological applications, as illustrated in Figure 19A [27, 69, 74, 121, 201]. There are several color centers in nanodiamonds that can be called NIR centers. For example, in addition to nitrogen-vacancy (NV) [27, 121], silicon-vacancy (SiV) [66, 206], tin-vacancy (SnV) [31], nickel-vacancy (NiV) [207, 208], and marginally germanium-vacancy (GeV) [209].

As stated above, the emission of the NV center is perfectly located within the biological transparency window as shown in Figure 19A, B [61]. However, the maximum of the absorption band (480–600 nm) of the NV color center overlaps with the biological tissues absorption band resulting in autofluorescence background [187, 210]. To overcome this drawback, recent reports have shown that the excitation bands of NV centers in certain micro and nanodiamonds can be extended to the zero-phonon wavelength of 638 nm and possibly beyond, which is in the region of suppressed autofluorescence of the biological

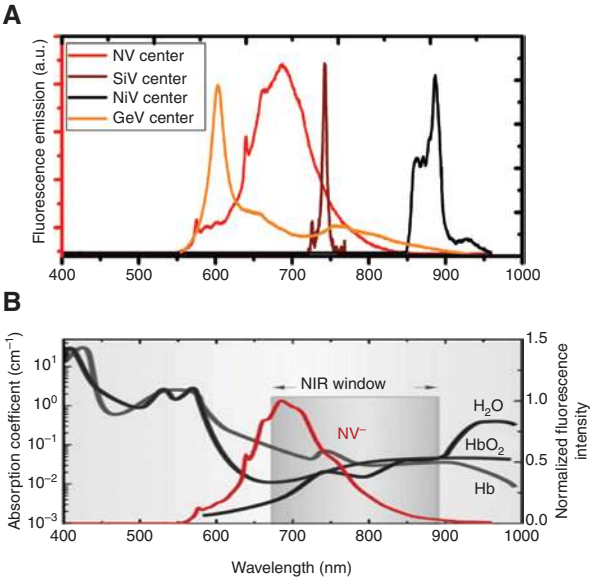

Figure 19: New fluorescent nanodiamonds in the biological transparency window.
(A) Superimposed photoluminescence spectra of color centers in nanodiamonds (FNDs), namely, germanium-vacancy (GeV), nitrogen-vacancy (NV), silicon-vacancy (SiV), and nickel-vacancy (NiV). (B) The fluorescence spectra of all diamond color centers in (a) fit within the biological transparency window. The black, dark gray, and light gray curves are the absorption spectra of H_2O, oxygen-bound hemoglobin (HbO_2), and hemoglobin (Hb), respectively. Adapted from [61].

tissue [132, 187]. This is a step forward to make NV centers more biocompatible for biological applications.

The silicon vacancy defect in diamond consists of a silicon atom and a split vacancy. It has both emission and absorption bands in the NIR spectral window. The photoluminescence (PL) of SiV displays a large spread of emission wavelengths (between 730 and 750 nm), but most of the emission lies within a fairly sharp zero-phonon line (ZPL) centered at around 738 nm, as shown in Figure 19A [29]. The optical excitation wavelength for the SiV color center can be easily selected within the NIR window [29] or in the visible. Notably, the SiV color center was reported as a stable fluorescent marker in ultra-small (1.2 nm) nanodiamond crystals [66].

The nickel color center (Ni) in diamond is a substitutional Ni site in the diamond lattice, which may also include a split vacancy. It possesses a strong photoluminescence (PL) doublet around 883/885 nm as shown in Figure 19A [207, 208], which is attributed to ground state splitting caused by the spin orbital interaction. Ni also has a biocompatible excitation range (650–800 nm), which makes it an excellent candidate for biological imaging and sensing applications.

Tin-vacancy (SnV) color center in diamond has been recently discovered [31]. Like the SiV, the tin atom sits on an interstitial site with two neighboring vacancies in the diamond crystal. It has been incorporated into diamond via ion implantation and subsequent high-temperature annealing. The SnV center exhibits a sharp zero phonon line at 619 nm at room temperature and then this line splits into four peaks at cryogenic temperatures due to a larger ground state splitting (~850 GHz). Furthermore, the excitation and emission of the SnV color center are located with the biological transparency window [31].

Germanium-vacancy (GeV) is a color center in diamonds, composed of a germanium (Ge) and a vacancy (V) [209] with a structure like the SiV. GeV exhibits a marginally biocompatible photoluminescence band (595–610 nm) with most of the emission concentrated in a zero-phonon line at 602 nm at room temperature [209]. The excitation wavelengths of GeV can be in green or red bands, which make it a potential fluorescent marker in bio-imaging and biomedical applications.

In general, elements heavier than Si, when implanted in diamond, are expected to give split vacancy structure like the SiV [34]. Based on recent work with Ge and Sn, and more recently Mg, it is estimated that many of these centers will have narrow emission lines in the visible to near IR range and will thus allow multiplexing with other fluorescent probes, as desired.

In summary, due to the growing number of NIR and visible color centers in nanodiamonds, as so far only a fraction of the periodic table has been implanted into diamond [34], they promise to be excellent candidates for high contrast fluorescent markers, even deep inside biological tissues when excited with biocompatible wavelengths (635–800 nm). It is important to know that most of the above mentioned color centers have still only been seen in bulk diamond and in relatively large nanodiamond crystals (>100 nm).

12 Future outlook for fluorescent nanodiamonds

Commercial nanodiamonds are fabricated by two main techniques: (1) crushing larger diamonds [211] and (2) detonation of explosives [63]. In addition, nanodiamonds are fabricated by non-detonation shock wave techniques such as laser ablation [212] and ultrasound [213]. There is also research in direct growth of nanodiamonds via CVD [214], and in flowing plasma [215], plus numerous other techniques. However, none of the existing nanodiamond fabrication techniques produces material that is close to the quality of bulk diamond, and this often leads to photostability problems for sizes less than 10 nm and sensitivity problems for NV centers [36].

Recently, in an attempt to overcome the limitations of ultrasmall nanodiamonds, direct growth starting from organic precursors has been performed at high-pressure high-temperature (HPHT) >900°C [216, 217], using techniques developed a long time ago [218]. So far, FNDs with NV and SiV color centers have been grown by these techniques. In addition, researchers have also been attempting to grow high-quality nanodiamonds around diamondoid seed molecules for more than a decade using CVD techniques. The motivation is that a diamondoid molecule is already like an ultrasmall diamond without defects, so that growing around a diamondoid seed molecule should give much higher quality nanodiamonds. Such seeded growth has successfully been applied to enhance nucleation of nanodiamonds for the growth of superior nanocrystal CVD diamond films [219–221]. Recently, the

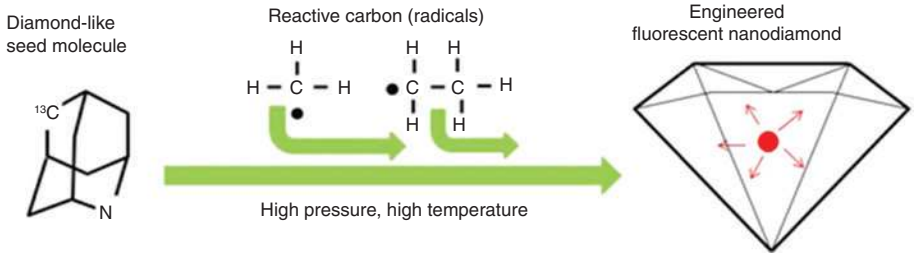

Figure 20: The basic concept of engineered fluorescent nanodiamonds via molecule seeded growth.
A diamond-like seed molecule is chosen that has specific atoms arranged in the approximate locations needed to form the color center of interest (the example shown is aza-adamantane with a 13C carbon that could be a precursor for a nitrogen-vacancy quantum register). Carbon radicals (like the methyl and ethyl radicals shown) are then created by cracking a hydrocarbon that decomposes at a much lower temperature than the diamondoid seed molecule. The subsequent growth of a diamond around the seed molecule gives a near-deterministic number and placement of the desired color center, and also assures at least one fluorescent emitter per nanodiamond no matter how small. Adapted from [224].

growth temperature has been reduced to well below the diamondoid decomposition temperature [220] in the hopes of improving yield (fraction of diamondoids producing diamonds). However, the yield is still extremely small (i.e. isolated nanodiamonds separated by microns compared to self-assembled seed layers with sub-nanometer separations).

Another work has shown that easily cracked isobutene molecules can serve as a source of reactive carbon in the synthesis of larger diamondoids from smaller ones [222], which presumably is a key intermediate step in the growth of nanodiamonds. This same work attempted seeded nanodiamond growth via CVD at a temperature below the seed decomposition temperature and observed enhanced nanodiamond films, but again with a relatively small yield. Finally, larger diamondoids have also been grown from smaller ones in xenon plasma, again with a rapidly decreasing yield as diamondoid order increases [223].

In addition to higher quality nanodiamonds, the diamondoid molecule seeding approach has the potential to deterministically produce color centers so that every nanodiamond, no matter how small, can have one or more bright fluorescent emitter [224]. This overcomes the limitation of all existing fabrication techniques including growth and post-implantation, which are inherently probabilistic in nature. Thus, instead of treating color center creation in nanodiamonds as a crystal growth or processing problem, it can be approached as a chemistry problem for seed molecule synthesis. This approach is illustrated in Figure 20. Here, the first step is to synthesize a molecule that will act as a precursor (or seed) for specific color centers [224]. A diamond will be grown around this molecule in a non-destructive way, so that the resulting nanodiamond (or micro-diamond) can have a completely independent chemical and isotopic composition from the seed molecule, yet still be a single crystal.

It is clear that this technique could be extended to other color centers. For example, a diamondoid seed with a single silicon atom could in principle form a 2-nm SiV nanodiamond, which reproduces the properties of the meteor diamonds (i.e. a photostable fluorescent diamond that is smaller than many protein based dyes) [66]. Also, more complex color centers may be possible. For example, one of the best diamond emitters consists of a nickel atom surrounded by four nitrogen atoms (NE8 center) [225]. It has strong narrowband emission in the tissue transparency window. This color center is not favored by probabilistic growth, but could in principle be grown with high yield by using the appropriate seed molecule. In summary, while the field of fluorescent nanodiamond has been limited by material quality and growth issues, these will likely soon be solved by the direct HPHT growth techniques starting from organic molecules, including the diamondoid molecule seeded growth approach.

Acknowledgment: This research is supported by a grant from King Abdulaziz City for Science and Technology (KACST). Also, we acknowledge the support of the TAMU CRI and GRUI grants, Air Force Office of Sponsored Research (Award No. FA9550-18-1-0141), the Office of Naval Research Grant N00014-16-1-3054, and the Robert A. Welch Foundation Award A1261. P.H. acknowledges financial support from the Government of the Russian Federation (Mega-grant No. 14.W03.31.0028).

References

[1] Gao L, Shao L, Chen B-C, Betzig E. 3D live fluorescence imaging of cellular dynamics using Bessel beam plane illumination microscopy. Nat Protoc 2014;9:1083–101.
[2] Gu L, Hall DJ, Qin Z, et al. In vivo time-gated fluorescence imaging with biodegradable luminescent porous silicon nanoparticles. Nat Commun 2013;4:2326.
[3] Juette MF, Terry DS, Wasserman MR, et al. The bright future of single-molecule fluorescence imaging. Curr Opin Chem Biol 2014;20:103–11.
[4] Keller PJ. Imaging morphogenesis: technological advances and biological insights. Science 2013;340:6137.
[5] Kusumi A, Tsunoyama TA, Hirosawa KM, Kasai RS, Fujiwara TK. Tracking single molecules at work in living cells. Nat Chem Biol 2014;10:524–32.
[6] Waggoner A. Fluorescent labels for proteomics and genomics. Curr Opin Chem Biol 2006;10:62–6.
[7] Kitai AH. Luminescent materials and applications. In: Wiley series in materials for electronic and optoelectronic applications. John Wiley & Sons, England, 2008, 278.
[8] Rurack K, Spieles M. Fluorescence quantum yields of a series of red and near-infrared dyes emitting at 600 – 1000 nm. Anal Chem 2011;83:1232–42.
[9] Polom K, Murawa D, Rho YS, Nowaczyk P, Hünerbein M, Murawa P. Current trends and emerging future of indocyanine green usage in surgery and oncology. Cancer 2011;117:4812–22.
[10] Soper SA, Mattingly QL. Steady-state and picosecond laser fluorescence studies of nonradiative pathways in tricarbocyanine dyes: implications to the design of near-IR fluorochromes with high fluorescence efficiencies. J Am Chem Soc 1994;116:3744–52.
[11] Luo S, Zhang E, Su Y, Cheng T, Shi C. A review of NIR dyes in cancer targeting and imaging. Biomaterials 2011;32:7127–38.
[12] Yarmoluk SM, Kovalska VB, Volkova KD. Optimized dyes for protein and nucleic acid detection. In: Demchenko AP, ed. Advanced fluorescence reporters in chemistry and biology III: applications in sensing and imaging. Berlin, Heidelberg, Springer, 2011, 161–99.
[13] Resch-Genger U, Grabolle M, Cavaliere-Jaricot S, Nitschke R, Nann T. Quantum dots versus organic dyes as fluorescent labels. Nat Methods 2008;5:763–75.

[14] Alivisatos AP. Semiconductor clusters, nanocrystals, and quantum dots. Science 1996;271:933–7.
[15] Wu C, Chiu DT. Highly fluorescent semiconducting polymer dots for biology and medicine. Angew Chem Int Ed Engl 2013;52:3086–109.
[16] Palantavida S, Peng B, Sokolov I. Ultrabright fluorescent silica particles with a large number of complex spectra excited with a single wavelength for multiplex applications. Nanoscale 2017;9:4881–90.
[17] Alkahtani MH, Gomes CL, Hemmer PR. Engineering water-tolerant core/shell upconversion nanoparticles for optical temperature sensing. Opt Lett 2017;42:2451–4.
[18] Alkahtani MH, Alghannam FS, Sanchez C, Gomes CL, Liang H, Hemmer PR. High efficiency upconversion nanophosphors for high-contrast bioimaging. Nanotechnology 2016;27:485501.
[19] Wang Y-F, Liu G-Y, Sun L-D, Xiao J-W, Zhou J-C, Yan C-H. Nd^{3+}-sensitized upconversion nanophosphors: efficient in vivo bioimaging probes with minimized heating effect. ACS Nano 2013;7:7200–6.
[20] Wolfbeis OS. An overview of nanoparticles commonly used in fluorescent bioimaging. Chem Soc Rev 2015;44:4743–68.
[21] Hong G, Diao S, Antaris AL, Dai H. Carbon nanomaterials for biological imaging and nanomedicinal therapy. Chem Rev 2015;115:10816–906.
[22] Montalti M, Cantelli A, Battistelli G. Nanodiamonds and silicon quantum dots: ultrastable and biocompatible luminescent nanoprobes for long-term bioimaging. Chem Soc Rev 2015;44:4853–921.
[23] Lewinski N, Colvin V, Drezek R. Cytotoxicity of nanoparticles. Small 2008;4:26–49.
[24] Cheng Y, Lu G, He Y, et al. Luminescence quantum yields of gold nanoparticles varying with excitation wavelengths. Nanoscale 2016;8:2188–94.
[25] Rao W, Li Q, Wang Y, Li T, Wu L. Comparison of photoluminescence quantum yield of single gold nanobipyramids and gold nanorods. ACS Nano 2015;9:2783–91.
[26] Zaitsev AM. Optical properties of diamond: a data handbook. Berlin, New York, Springer 2001, xvii, 502 p.
[27] Hsiao WW, Hui YY, Tsai PC, Chang HC. Fluorescent nanodiamond: a versatile tool for long-term cell tracking, super-resolution imaging, and nanoscale temperature sensing. Acc Chem Res 2016;49:400–7.
[28] Reineck P, Francis A, Orth A, et al. Brightness and photostability of emerging red and near-IR fluorescent nanomaterials for bioimaging. Adv Opt Mater 2016;4:1549–57.
[29] Schirhagl R, Chang K, Loretz M, Degen CL. Nitrogen-vacancy centers in diamond: nanoscale sensors for physics and biology. Annu Rev Phys Chem 2014;65:83–105.
[30] Wu Y, Jelezko F, Plenio MB, Weil T. Diamond quantum devices in biology. Angew Chem Int Ed Engl 2016;55:6586–98.
[31] Iwasaki T, Miyamoto Y, Taniguchi T, et al. Tin-vacancy quantum emitters in diamond. Phys Rev Lett 2017;119:253601.
[32] Aharonovich I, Neu E. Diamond nanophotonics. Adv Opt Mater 2014;2:911–28.
[33] Smith AM, Nie S. Chemical analysis and cellular imaging with quantum dots. Analyst 2004;129:672–7.
[34] Zaitsev AM. Vibronic spectra of impurity-related optical centers in diamond. Phys Rev B 2000;61:12909–22.
[35] Genovese D, Bonacchi S, Juris R, et al. Prevention of self-quenching in fluorescent silica nanoparticles by efficient energy transfer. Angew Chem Int Ed Engl 2013;52:5965–8.
[36] Shenderova O, Nunn N, Oeckinghaus T, et al. Commercial quantities of ultrasmall fluorescent nanodiamonds containing color centers. In: Proceedings Volume 10118, Advances in Photonics of Quantum Computing, Memory, and Communication X, 2017, 1011803.
[37] Barbagiovanni EG, Lockwood DJ, Simpson PJ, Goncharova LV. Quantum confinement in Si and Ge nanostructures. J Appl Phys 2012;111:034307.
[38] Klimov VI, Ivanov SA, Nanda J, et al. Single-exciton optical gain in semiconductor nanocrystals. Nature 2007;447:441–6.
[39] Takagahara T, Takeda K. Theory of the quantum confinement effect on excitons in quantum dots of indirect-gap materials. Phys Rev B: Condens Matter 1992;46:15578–81.
[40] Murphy CJ. Optical sensing with quantum dots. Anal Chem 2002;74:520a–6a.
[41] Wang X, Ren X, Kahen K, et al. Non-blinking semiconductor nanocrystals. Nature 2009;459:686–9.
[42] Wang X, Ren X, Kahen K, et al. Retraction: non-blinking semiconductor nanocrystals. Nature 2015;527:544.
[43] Tsoi KM, Dai Q, Alman BA, Chan WC. Are quantum dots toxic? Exploring the discrepancy between cell culture and animal studies. Acc Chem Res 2013;46:662–71.
[44] Chang E, Thekkek N, Yu WW, Colvin VL, Drezek R. Evaluation of quantum dot cytotoxicity based on intracellular uptake. Small 2006;2:1412–7.
[45] Oh E, Liu R, Nel A, et al. Meta-analysis of cellular toxicity for cadmium-containing quantum dots. Nat Nanotechnol 2016;11:479–86.
[46] Lin YC, Wu KT, Lin ZR, et al. Nanodiamond for biolabelling and toxicity evaluation in the zebrafish embryo in vivo. J Biophotonics 2016;9:827–36.
[47] Mohan N, Chen C-S, Hsieh H-H, Wu Y-C, Chang H-C. In vivo imaging and toxicity assessments of fluorescent n anodiamonds in *Caenorhabditis elegans*. Nano Lett 2010;10:3692–9.
[48] Yu S-J, Kang M-W, Chang H-C, Chen K-M, Yu Y-C. Bright fluorescent nanodiamonds: no photobleaching and low cytotoxicity. J Am Chem Soc 2005;127:17604–5.
[49] Lewis EK, Haaland WC, Nguyen F, et al. Color-blind fluorescence detection for four-color DNA sequencing. Proc Natl Acad Sci USA 2005;102:5346–51.
[50] Xu S, Kumar S, Nann T. Rapid synthesis of high-quality InP nanocrystals. J Am Chem Soc 2006;128:1054–5.
[51] Liu F, Ye W, Wang J, et al. Parallel comparative studies on toxicity of quantum dots synthesized and surface engineered with different methods in vitro and in vivo. Int J Nanomed 2017;12:5135–48.
[52] Wehling J, Dringen R, Zare RN, Maas M, Rezwan K. Bactericidal activity of partially oxidized nanodiamonds. ACS Nano 2014;8:6475–83.
[53] Jarre G, Liang Y, Betz P, Lang D, Krueger A. Playing the surface game-Diels-Alder reactions on diamond nanoparticles. Chem Commun 2011;47:544–6.
[54] Liang Y, Meinhardt T, Jarre G, et al. Deagglomeration and surface modification of thermally annealed nanoscale diamond. J Colloid Interface Sci 2011;354:23–30.
[55] Turcheniuk K, Vadym NM. Biomedical applications of nanodiamond (Review). Nanotechnology 2017;28:252001.
[56] Kruger A, Liang Y, Jarre G, Stegk J. Surface functionalisation of detonation diamond suitable for biological applications. J Mater Chem 2006;16:2322–8.

[57] Huang LCL, Chang H-C. Adsorption and immobilization of cytochrome c on nanodiamonds. Langmuir 2004;20:5879–84.
[58] Kossovsky N, Gelman A, Hnatyszyn HJ, et al. Surface-modified diamond nanoparticles as antigen delivery vehicles. Bioconjug Chem 1995;6:507–11.
[59] Ushizawa K, Sato Y, Mitsumori T, et al. Covalent immobilization of DNA on diamond and its verification by diffuse reflectance infrared spectroscopy. Chem Phys Lett 2002;351:105–8.
[60] Havlik J, Raabova H, Gulka M, et al. Benchtop fluorination of fluorescent nanodiamonds on a preparative scale: toward unusually hydrophilic bright particles. Adv Funct Mater 2016;26:4134–42.
[61] Vaijayanthimala V, Cheng PY, Yeh SH, et al. The long-term stability and biocompatibility of fluorescent nanodiamond as an in vivo contrast agent. Biomaterials 2012;33:7794–802.
[62] Schrand AM, Hens SAC, Shenderova OA. Nanodiamond particles: properties and perspectives for bioapplications. Crit Rev Solid State Mater Sci 2009;34:18–74.
[63] Mochalin VN, Shenderova O, Ho D, Gogotsi Y. The properties and applications of nanodiamonds. Nat Nanotechnol 2011;7:11–23.
[64] Boudou J-P, Curmi PA, Jelezko F, et al. High yield fabrication of fluorescent nanodiamonds. Nanotechnology 2009;20:235602.
[65] Yu M, Zheng J. Clearance pathways and tumor targeting of imaging nanoparticles. ACS Nano 2015;9:6655–74.
[66] Vlasov II, Shiryaev AA, Rendler T, et al. Molecular-sized fluorescent nanodiamonds. Nat Nanotechnol 2014;9:54–8.
[67] Huang H, Pierstorff E, Osawa E, Ho D. Active nanodiamond hydrogels for chemotherapeutic delivery. Nano Lett 2007;7:3305–14.
[68] Chow EK, Zhang XQ, Chen M, et al. Nanodiamond therapeutic delivery agents mediate enhanced chemoresistant tumor treatment. Sci Transl Med 2011;3:73ra21.
[69] Wu Y, Weil T. Nanodiamonds for biological applications. Phys Sci Rev 2017;2:0104.
[70] Landeros-Mart L-L, Chavez-Flores D, Orrantia-Borunda E, Flores-Holguin N. Construction of a nanodiamond–tamoxifen complex as a breast cancer drug delivery vehicle. J Nanomater 2016; Article ID 2682105, 9 p.
[71] Guan B, Zou F, Zhi J. Nanodiamond as the pH-responsive vehicle for an anticancer drug. Small 2010;6:1514–9.
[72] Chen M, Pierstorff ED, Lam R, et al. Nanodiamond-mediated delivery of water-insoluble therapeutics. ACS Nano 2009;3:2016–22.
[73] Toh T-B, Lee DK, Hou W, et al. Nanodiamond–mitoxantrone complexes enhance drug retention in chemoresistant breast cancer cells. Mol Pharm 2014;11:2683–91.
[74] Shimkunas RA, Robinson E, Lam R, et al. Nanodiamond–insulin complexes as pH-dependent protein delivery vehicles. Biomaterials 2009;30:5720–8.
[75] Friedman CM, Sandrik JL, Heuer MA, Rapp GW. Composition and mechanical properties of gutta-percha endodontic points. J Dent Res 1975;54:921–5.
[76] Clinton K, Van Himel T. Comparison of a warm gutta-percha obturation technique and lateral condensation. J Endod 2001;27:692–5.
[77] Soo WK, Thong YL, Gutmann JL. A comparison of four gutta-percha filling techniques in simulated C-shaped canals. Int Endod J 2015;48:736–46.
[78] Lee D-K, Kee T, Liang Z, et al. Clinical validation of a nanodiamond-embedded thermoplastic biomaterial. Proc Natl Acad Sci USA 2017;114:E9445–54.
[79] Hong C, Song D, Lee DK, et al. Reducing posttreatment relapse in cleft lip palatal expansion using an injectable estrogen-nanodiamond hydrogel. Proc Natl Acad Sci USA 2017;114:E7218–25.
[80] Stoll C, Alembik Y, Dott B, Roth MP. Associated malformations in cases with oral clefts. Cleft Palate Craniofac J 2000;37:41–7.
[81] Arosarena OA. Cleft lip and palate. Otolaryngol Clin North Am 2007;40:27–60, vi.
[82] Moussa R, O'Reilly MT, Close JM. Long-term stability of rapid palatal expander treatment and edgewise mechanotherapy. Am J Orthod Dentofacial Orthop 1995;108:478–88.
[83] Stockfisch H. Rapid expansion of the maxilla – success and relapse. Rep Congr Eur Orthod Soc 1969:469–81.
[84] Slegerova J, Hajek M, Rehor I, et al. Designing the nanobiointerface of fluorescent nanodiamonds: highly selective targeting of glioma cancer cells. Nanoscale 2015;7:415–20.
[85] Wu Y, Ermakova A, Liu W, et al. Programmable biopolymers for advancing biomedical applications of fluorescent nanodiamonds. Adv Funct Mater 2015;25:6576–85.
[86] Reineck P, Lau DWM, Wilson ER, Nunn N, Shenderova OA, Gibson BC. Visible to near-IR fluorescence from single-digit detonation nanodiamonds: excitation wavelength and pH dependence. Sci Rep 2018;8:2478.
[87] Visscher K, Schnitzer MJ, Block SM. Single kinesin molecules studied with a molecular force clamp. Nature 1999;400:184–9.
[88] Sheetz MP, Spudich JA. Movement of myosin-coated fluorescent beads on actin cables in vitro. Nature 1983;303:31–5.
[89] Eid J, Fehr A, Gray J, et al. Real-time DNA sequencing from single polymerase molecules. Science 2009;323:133–8.
[90] Michalet X, Pinaud FF, Bentolila LA, et al. Quantum dots for live cells, in vivo imaging, and diagnostics. Science 2005;307:538–44.
[91] Saxton MJ, Jacobson K. Single-particle tracking: applications to membrane dynamics. Annu Rev Biophys Biomol Struct 1997;26:373–99.
[92] Xu R, Huang L, Wei W, Chen X, Zhang X, Zhang X. Real-time imaging and tracking of ultrastable organic dye nanoparticles in living cells. Biomaterials 2016;93:38–47.
[93] Chang Y-P, Pinaud F, Antelman J, Weiss S. Tracking biomolecules in live cells using quantum dots. J Biophotonics 2008;1:287–98.
[94] Gardini L, Capitanio M, Pavone FS. 3D tracking of single nanoparticles and quantum dots in living cells by out-of-focus imaging with diffraction pattern recognition. Sci Rep 2015;5:Article number 16088.
[95] Idris NM, Li Z, Ye L, Sim EK, Mahendran R, Ho PC, Zhang Y. Tracking transplanted cells in live animal using upconversion fluorescent nanoparticles. Biomaterials 2009;30:5104–13.
[96] Fu CC, Lee H-Y, Chen K, et al. Characterization and application of single fluorescent nanodiamonds as cellular biomarkers. Proc Natl Acad Sci USA 2007;104:727–32.
[97] Chang YR, Lee H-Y, Chen K, et al. Mass production and dynamic imaging of fluorescent nanodiamonds. Nat Nanotechnol 2008;3:284–8.
[98] McGuinness LP, Yan Y, Stacey A, et al. Quantum measurement and orientation tracking of fluorescent nanodiamonds inside living cells. Nat Nanotechnol 2011;6:358–63.

[99] Hossain FM, Doherty MW, Wilson HF, Hollenberg LC. Ab initio electronic and optical properties of the N-v-center in diamond. Phys Rev Lett 2008;101:226403.
[100] Hall LT, Hill CD, Cole JH, et al. Monitoring ion-channel function in real time through quantum decoherence. Proc Natl Acad Sci USA 2010;107:18777–82.
[101] Hanson R, Dobrovitski VV, Feiguin AE, Gywat O, Awschalom DD. Coherent dynamics of a single spin interacting with an adjustable spin bath. Science 2008;320:352–5.
[102] Haziza S, Mohan N, Loe-Mie Y, et al. Fluorescent nanodiamond tracking reveals intraneuronal transport abnormalities induced by brain-disease-related genetic risk factors. Nat Nanotechnol 2017;12:322–8.
[103] McClellan J, King MC. Genetic heterogeneity in human disease. Cell 2010;141:210–7.
[104] Hirokawa N, Niwa S, Tanaka Y. Molecular motors in neurons: transport mechanisms and roles in brain function, development, and disease. Neuron 2010;68:610–38.
[105] Millecamps S, Julien JP. Axonal transport deficits and neurodegenerative diseases. Nat Rev Neurosci 2013;14:161–76.
[106] Kwinter DM, Lo K, Mafi P, Silverman MA. Dynactin regulates bidirectional transport of dense-core vesicles in the axon and dendrites of cultured hippocampal neurons. Neuroscience 2009;162:1001–10.
[107] Pinaud F, Clarke S, Sittner A, Dahan M. Probing cellular events, one quantum dot at a time. Nat Methods 2010;7:275–85.
[108] Doudna JA, Charpentier E. Genome editing. The new frontier of genome engineering with CRISPR-Cas9. Science 2014;346:1258096.
[109] Alkahtani M, Jiang L, Brick R, Hemmer P, Scully M. Nanometer-scale luminescent thermometry in bovine embryos. Opt Lett 2017;42:4812–5.
[110] Wang L, Liu Y, Li W, et al. Selective targeting of gold nanorods at the mitochondria of cancer cells: implications for cancer therapy. Nano Lett 2011;11:772–80.
[111] Morille M, Passirani C, Vonarbourg A, Clavreul A, Benoit JP. Progress in developing cationic vectors for non-viral systemic gene therapy against cancer. Biomaterials 2008;29:3477–96.
[112] Wang, L, Jiang X, Ji Y, et al. Surface chemistry of gold nanorods: origin of cell membrane damage and cytotoxicity. Nanoscale 2013;5:8384–91.
[113] Chu Z, Zhang S, Zhang B, et al. Unambiguous observation of shape effects on cellular fate of nanoparticles. Sci Rep 2014;4:4495.
[114] Chu Z, Miu K, Lung P, et al. Rapid endosomal escape of prickly nanodiamonds: implications for gene delivery. Sci Rep 2015;5:Article number: 11661.
[115] Jaque D, Vetrone F. Luminescence nanothermometry. Nanoscale 2012;4:4301–26.
[116] Yang J-M, Yang H, Lin L. Quantum dot nano thermometers reveal heterogeneous local thermogenesis in living cells. ACS Nano 2011;5:5067–71.
[117] Vetrone F, Naccache R, Zamarrón A, et al. Temperature sensing using fluorescent nanothermometers. ACS Nano 2010;4:3254–8.
[118] Donner JS, Thompson SA, Kreuzer MP, Baffou G, Quidant R. Mapping intracellular temperature using green fluorescent protein. Nano Lett 2012;12:2107–11.
[119] Okabe K, Inada N, Gota C, Harada Y, Funatsu T, Uchiyama S. Intracellular temperature mapping with a fluorescent polymeric thermometer and fluorescence lifetime imaging microscopy. Nat Commun 2012;3: Article number: 705.
[120] Kucsko G, Maurer PC, Yao NY, et al. Nanometre-scale thermometry in a living cell. Nature 2013;500:54–8.
[121] Neumann P, Jakobi I, Dolde F, et al. High-precision nanoscale temperature sensing using single defects in diamond. Nano Lett 2013;13:2738–42.
[122] Toyli DM, de las Casas CF, Christle DJ, Dobrovitski VV, Awschalom DD. Fluorescence thermometry enhanced by the quantum coherence of single spins in diamond. Proc Natl Acad Sci USA 2013;110:8417–21.
[123] Plakhotnik T, Doherty MW, Cole JH, Chapman R, Manson NB. All-optical thermometry and thermal properties of the optically detected spin resonances of the NV^- center in nanodiamond. Nano Lett 2014;14:4989–96.
[124] Tzeng Y-K, Tsai P-C, Liu H-Y, et al. Time-resolved luminescence nanothermometry with nitrogen-vacancy centers in nanodiamonds. Nano Lett 2015;15:3945–52.
[125] Wang N, Liu G-Q, Leong W-H, et al. Magnetic criticality-enhanced hybrid nanodiamond-thermometer under ambient conditions. arXiv preprint arXiv:1707.02885, 2017.
[126] Nguyen CT, Evans RE, Sipahigil A, et al. All-optical nanoscale thermometry with silicon-vacancy centers in diamond. Appl Phys Lett 2018;112:203102.
[127] Fan J-W, Cojocaru I, Becker J, et al. Germanium-vacancy color center in diamond as a temperature sensor. ACS Photon 2018;5:765–70.
[128] Baffou G, Rigneault H, Marguet D, Jullien L. A critique of methods for temperature imaging in single cells. Nat Methods 2014;11:899–901.
[129] Gracheva EO, Cordero-Morales JF, González-Carcacía JA, et al. Ganglion-specific splicing of TRPV1 underlies infrared sensation in vampire bats. Nature 2011;476:88–91.
[130] Vriens J, Nilius B, Voets T. Peripheral thermosensation in mammals. Nat Rev Neurosci 2014;15:573–89.
[131] McKemy DD, Neuhausser WM, Julius D. Identification of a cold receptor reveals a general role for TRP channels in thermosensation. Nature 2002;416:52–8.
[132] Lanin AA, Fedotov IV, Ermakova YG, et al. Fiber-optic electron-spin-resonance thermometry of single laser-activated neurons. Opt Lett 2016;41:5563–6.
[133] Masters BR. Fluorescence microscopy: from principles to biological applications. J Biomed Opt 2014;19:049901.
[134] Zhehai Z, Lianqing Z. STED microscopy based on axially symmetric polarized vortex beams. Chin Phys B 2016;25:030701.
[135] Rittweger E, Han KY, Irvine SE, Eggeling C, Hell SW. STED microscopy reveals crystal colour centres with nanometric resolution. Nat Photon 2009;3:144–7.
[136] Han KY, Willig KI, Rittweger E, et al. Three-dimensional stimulated emission depletion microscopy of nitrogen-vacancy centers in diamond using continuous-wave light. Nano Lett 2009;9:3323–9.
[137] Tzeng Y-K, Faklaris O, Chang B-M, Kuo Y, Hsu J-H, Chang H-C. Superresolution imaging of albumin-conjugated fluorescent nanodiamonds in cells by stimulated emission depletion. Angew Chem Int Ed 2011;50:2262–5.
[138] Arroyo-Camejo S, Adam M-P, Besbes M, et al. Stimulated emission depletion microscopy resolves individual nitrogen vacancy centers in diamond nanocrystals. ACS Nano 2013;7:10912–9.

[139] Hong S, Grinolds MS, Pham LM, et al. Nanoscale magnetometry with NV centers in diamond. MRS Bulletin 2013; 38:155–61.
[140] Dolde F, Fedder H, Doherty MW, et al. Electric-field sensing using single diamond spins. Nat Phys 2011;7:459–63.
[141] Toyli DM, Christle DJ, Alkauskas A, et al. Measurement and control of single nitrogen-vacancy center spins above 600 K. Phys Rev X 2012;2:031001.
[142] Maze JR, Stanwix PL, Hodges JS, et al. Nanoscale magnetic sensing with an individual electronic spin in diamond. Nature 2008;455:644–7.
[143] Balasubramanian G, Neumann P, Twitchen D, et al. Ultralong spin coherence time in isotopically engineered diamond. Nat Mater 2009;8:383–7.
[144] Balasubramanian G, Chan IY, Kolesov R, et al. Nanoscale imaging magnetometry with diamond spins under ambient conditions. Nature 2008;455:648–51.
[145] Hall LT, Beart GC, Thomas EA, et al. High spatial and temporal resolution wide-field imaging of neuron activity using quantum NV-diamond. Sci Rep 2012;2:401.
[146] Acosta VM, Bauch E, Ledbetter MP, Waxman A, Bouchard L-S, Budker D. Temperature dependence of the nitrogen-vacancy magnetic resonance in diamond. Phys Rev Lett 2010;104:070801.
[147] Wang J, Feng F, Zhang J, et al. High-sensitivity temperature sensing using an implanted single nitrogen-vacancy center array in diamond. Phys Rev B 2015;91:155404.
[148] Jianming C, Jelezko F, Plenio MB, Retzker A. Diamond-based single-molecule magnetic resonance spectroscopy. New J Phys 2013;15:013020.
[149] Hall LT, Cole JH, Hill CD, Hollenberg LCL. Sensing of fluctuating nanoscale magnetic fields using nitrogen-vacancy centers in diamond. Phys Rev Lett 2009;103:220802.
[150] Cole JH, Hollenberg LC. Scanning quantum decoherence microscopy. Nanotechnology 2009;20:495401.
[151] Ermakova A, Pramanik G, Cai J-M, et al. Detection of a few metallo-protein molecules using color centers in nanodiamonds. Nano Lett 2013;13:3305–9.
[152] Sushkov AO, Chisholm N, Lovchinsky I, et al. All-optical sensing of a single-molecule electron spin. Nano Lett 2014;14:6443–8.
[153] Hemmer P, Gomes C. Single proteins under a diamond spotlight. Science 2015;347:1072–3.
[154] Degen CL, Poggio M, Mamin HJ, Rettner CT, Rugar D. Nanoscale magnetic resonance imaging. Proc Natl Acad Sci USA 2009;106:1313–7.
[155] Shi F, Zhang Q, Wang P, et al. Single-protein spin resonance spectroscopy under ambient conditions. Science 2015;347:1135–8.
[156] Bernhard G, Beck J, Neumann P, et al. Sensing external spins with nitrogen-vacancy diamond. New J Phys 2011;13:055004.
[157] Staudacher T, Shi F, Pezzagna S, et al. Nuclear magnetic resonance spectroscopy on a (5-Nanometer)^3 sample volume. Science 2013;339:561–3.
[158] Müller C, Kong X, Cai J-M, et al. Nuclear magnetic resonance spectroscopy with single spin sensitivity. Nat Commun 2014;5:4703.
[159] Lovchinsky I, Sushkov AO, Urbach E, et al. Nuclear magnetic resonance detection and spectroscopy of single proteins using quantum logic. Science 2016;351:836–41.
[160] Armstrong BD, Han S. A new model for Overhauser enhanced nuclear magnetic resonance using nitroxide radicals. J Chem Phys 2007;127:104508.
[161] Gunther UL. Dynamic nuclear hyperpolarization in liquids. Top Curr Chem 2013;335:23–69.
[162] Fischer AE, Hall LD. Roles for paramagnetic substances in MRI: contrast agents, molecular amplifiers, and indicators for redox and pH mapping. Magn Reson Mater Phys Biol Med 1994;2:203–10.
[163] Cassidy MC, Chan HR, Ross BD, Bhattacharya PK, Marcus CM. In vivo magnetic resonance imaging of hyperpolarized silicon particles. Nat Nanotechnol 2013;8:363–8.
[164] Manus LM, Mastarone DJ, Waters EA, et al. Gd(III)-nanodiamond conjugates for MRI contrast enhancement. Nano Lett 2010;10:484–9.
[165] McDonald RJ, McDonald JS, Kallmes DF, et al. Intracranial gadolinium deposition after contrast-enhanced MR imaging. Radiology 2015;275:772–82.
[166] Waddington DEJ, Sarracanie M, Zhang H, et al. Nanodiamond-enhanced MRI via in situ hyperpolarization. Nat Commun 2017;8: Article number: 15118.
[167] Lurie DJ, Li H, Petryakov S, Zweier JL. Development of a PEDRI free-radical imager using a 0.38 T clinical MRI system. Magn Reson Med 2002;47:181–6.
[168] Golman K, Leunbach I, Petersson JS, Holz D, Overweg J. Overhauser-enhanced MRI. Acad Radiol 2002; 9(Suppl 1):S104–8.
[169] Koonjoo N, Parzy E, Massot P, et al. In vivo Overhauser-enhanced MRI of proteolytic activity. Contrast Media Mol Imaging 2014;9:363–71.
[170] Ichikawa K, Yasukawa K. Imaging in vivo redox status in high spatial resolution with OMRI. Free Rad Res 2012; 46:1004–10.
[171] Sarracanie M, Armstrong BD, Stockmann J, Rosen MS. High speed 3D overhauser-enhanced MRI using combined b-SSFP and compressed sensing. Magn Reson Med 2014;71:735–45.
[172] Clarkson RB, Odintsov BM, Ceroke PJ, Ardenkjaer-Larsen JH, Fruianu M, Belford RL. Electron paramagnetic resonance and dynamic nuclear polarization of char suspensions: surface science and oximetry. Phys Med Biol 1998;43:1907–20.
[173] Ardenkjær-Larsen JH, Laursen I, Leunbach I, et al. EPR and DNP properties of certain novel single electron contrast agents intended for oximetric imaging. J Magn Reson 1998;133:1–12.
[174] Jochen S, Schwartz I, Chen Q, et al. Optically induced dynamic nuclear spin polarisation in diamond. New J Phys 2016;18:013040.
[175] King JP, Coles PJ, Reimer JA. Optical polarization of ^{13}C nuclei in diamond through nitrogen vacancy centers. Phys Rev B 2010;81:073201.
[176] Rej E, Gaebel T, Boele T, Waddington DEJ, Reilly DJ. Hyperpolarized nanodiamond with long spin-relaxation times. Nat Commun 2015;6:8459.
[177] King JP, Jeong K, Vassiliou CC, et al. Room-temperature in situ nuclear spin hyperpolarization from optically pumped nitrogen vacancy centres in diamond. Nat Commun 2015;6: Article number: 8965.
[178] Casabianca LB, Shames AI, Panich AM, Shenderova O, Frydman L. Factors affecting DNP NMR in polycrystalline diamond samples. J Phys Chem C 2011;115:19041–8.

[179] Dutta P, Martinez GV, Gillies RJ. Nanodiamond as a new hyperpolarizing agent and its ^{13}C MRS. J Phys Chem Lett 2014;5:597–600.
[180] James ML, Gambhir SS. A molecular imaging primer: modalities, imaging agents, and applications. Physiol Rev 2012;92:897–965.
[181] Levin CS. Primer on molecular imaging technology. Eur J Nucl Med Mol Imaging 2005;32:S325–45.
[182] Sosnovik D, Weissleder R. Magnetic resonance and fluorescence based molecular imaging technologies. Imaging Drug Discov Early Clin Trials 2005;62:83–115.
[183] Hahn MA, Singh AK, Sharma P, Brown SC, Moudgil BM. Nanoparticles as contrast agents for in-vivo bioimaging: current status and future perspectives. Anal Bioanal Chem 2011;399:3–27.
[184] Taylor JM, Cappellaro P, Childress L, et al. High-sensitivity diamond magnetometer with nanoscale resolution. Nat Phys 2008;4:810–6.
[185] Ruan Y, Simpson DA, Jeske J, et al. Remote nanodiamond magnetometry. arXiv preprint arXiv:1602.06611, 2016.
[186] Horowitz VR, Alemán BJ, Christle DJ, Cleland AN, Awschalom DD. Electron spin resonance of nitrogen-vacancy centers in optically trapped nanodiamonds. Proc Natl Acad Sci USA 2012;109:13493–7.
[187] Hegyi A, Yablonovitch E. Molecular imaging by optically detected electron spin resonance of nitrogen-vacancies in nanodiamonds. Nano Lett 2013;13:1173–8.
[188] Singam SKR, Motylewski J, Monaco A, et al. Contrast induced by a static magnetic field for improved detection in nanodiamond fluorescence microscopy. Phys Rev Appl 2016;6:064013.
[189] Arias E, Méndez MT, Arias E, et al. Supramolecular recognition of *Escherichia coli* bacteria by fluorescent oligo(phenyleneethynylene)s with mannopyranoside termini groups. Sensors 2017;17:1025.
[190] Yang W, Gelles J, Musser SM. Imaging of single-molecule translocation through nuclear pore complexes. Proc Natl Acad Sci USA 2004;101:12887–92.
[191] Prasher DC, Eckenrode VK, Ward WW, Prendergast FG, Cormier MJ. Primary structure of the Aequorea victoria green-fluorescent protein. Gene 1992;111:229–33.
[192] Xue X, Pan J, Xie H, Wang J, Zhang S. Fluorescence detection of total count of *Escherichia coli* and *Staphylococcus aureus* on water-soluble CdSe quantum dots coupled with bacteria. Talanta 2009;77:1808–13.
[193] Funatsu T, Taniyama T, Tajima T, Tadakuma H, Namiki H. Rapid and sensitive detection method of a bacterium by using a GFP reporter phage. Microbiol Immunol 2002;46:365–9.
[194] Edgar R, McKinstry M, Hwang J, et al. High-sensitivity bacterial detection using biotin-tagged phage and quantum-dot nanocomplexes. Proc Natl Acad Sci USA 2006;103:4841–5.
[195] Chao J-I, Perevedentseva E, Chung PH, et al. Nanometer-sized diamond particle as a probe for biolabeling. Biophys J 2007;93:2199–208.
[196] Elizabeth K, De Vos D, Gvasalia G, et al. Phage therapy in clinical practice: treatment of human infections. Curr Pharm Biotechnol 2010;11:69–86.
[197] Goodridge L, Chen J, Griffiths M. The use of a fluorescent bacteriophage assay for detection of Escherichia coli O157:H7 in inoculated ground beef and raw milk. Int J Food Microbiol 1999;47:43–50.
[198] Goodridge L, Chen J, Griffiths M. Development and characterization of a fluorescent-bacteriophage assay for detection of Escherichia coli O157:H7. Appl Environ Microbiol 1999;65:1397–404.
[199] Fu C-C, Lee H-Y, Chen K, et al. Characterization and application of single fluorescent nanodiamonds as cellular biomarkers. Proc Natl Acad Sci USA 2007;104:727–32.
[200] Cheng C-Y, Perevedentseva E, Tu J-S, Chung P-H, Cheng C-L. Direct and in vitro observation of growth hormone receptor molecules in A549 human lung epithelial cells by nanodiamond labeling. Appl Phys Lett 2007;90:163903.
[201] Kuang-Kai L, Cheng C-L, Chang C-C, Chao J-I. Biocompatible and detectable carboxylated nanodiamond on human cell. Nanotechnology 2007;18:325102.
[202] Trinh JT, Alkahtani MH, Rampersaud I, et al. Fluorescent nanodiamond-bacteriophage conjugates maintain host specificity. Biotechnol Bioeng 2018;115:1427–36.
[203] Bradac C, Gaebel T, Naidoo N, Rabeau JR, Barnard AS. Prediction and measurement of the size-dependent stability of fluorescence in diamond over the entire nanoscale. Nano Lett 2009;9:3555–64.
[204] Shu X, Shaner NC, Yarbrough CA, Tsien RY, Remington SJ. Novel chromophores and buried charges control color in mFruits. Biochemistry 2006;45:9639–47.
[205] Piatkevich KD, Malashkevich VN, Almo SC, Verkhusha VV. Engineering ESPT pathways based on structural analysis of lssmkate red fluorescent proteins with large stokes shift. J Am Chem Soc 2010;132:10762–70.
[206] Uwe J, Kurz AB, Rudnicki DS, et al. Nanodiamonds carrying silicon-vacancy quantum emitters with almost lifetime-limited linewidths. New J Phys 2016;18:073036.
[207] Aharonovich I, Zhou C, Stacey A, et al. Enhanced single-photon emission in the near infrared from a diamond color center. Phys Rev B 2009;79:235316.
[208] Nazare MH, Neves AJ, Davies G. Optical studies of the 1.40-eV Ni center in diamond. Phys Rev B Condens Matter 1991;43:14196–205.
[209] Iwasaki T, Ishibashi F, Miyamoto Y, et al. Germanium-vacancy single color centers in diamond. Sci Rep 2015;5: Article number: 12882.
[210] Igarashi R, Yoshinari Y, Yokota H, et al. Real-time background-free selective imaging of fluorescent nanodiamonds in vivo. Nano Lett 2012;12:5726–32.
[211] Tisler J, Balasubramanian G, Naydenov B, et al. Fluorescence and spin properties of defects in single digit nanodiamonds. ACS Nano 2009;3:1959–65.
[212] Amans D, Chenus A-C, Ledoux G, et al. Nanodiamond synthesis by pulsed laser ablation in liquids. Diam Relat Mater 2009;18:177–80.
[213] Khachatryan AK, Aloyan SG, May PW, Sargsyan R, Khachatryan VA, Baghdasaryan VS. Graphite-to-diamond transformation induced by ultrasound cavitation. Diam Relat Mater 2008;17:931–6.
[214] Elke N, Steinmetz D, Riedrich-Möller J, et al. Single photon emission from silicon-vacancy colour centres in chemical vapour deposition nano-diamonds on iridium. New J Phys 2011;13:025012.
[215] Kumar A, Lin PA, Xue A, Hao B, Yap YK, Mohan Sankaran R. Formation of nanodiamonds at near-ambient conditions via microplasma dissociation of ethanol vapour. Nat Commun 2013;4: Article number: 2618.

[216] Davydov VA, Rakhmanina AV, Agafonov VN, Khabashesku VN. Synergistic effect of fluorine and hydrogen on processes of graphite and diamond formation from fluorographite-naphthalene mixtures at high pressures. J Phys Chem C 2011;115:21000–8.
[217] Davydov VA, Rakhmanina AV, Lyapin SG, et al. Production of nano- and microdiamonds with Si-V and N-V luminescent centers at high pressures in systems based on mixtures of hydrocarbon and fluorocarbon compounds. JETP Lett 2014;99:585–9.
[218] Wentorf RH. The behavior of some carbonaceous materials at very high pressures and high temperatures. J Phys Chem 1965;69:3063–9.
[219] Zhang JL, Ishiwata H, Babinec TM, et al. Hybrid Group IV nanophotonic structures incorporating diamond silicon-vacancy color centers. Nano Lett 2016;16:212–7.
[220] Tzeng Y-K, Zhang JL, Lu H, et al. Vertical-substrate MPCVD epitaxial nanodiamond growth. Nano Lett 2017;17:1489–95.
[221] Ishiwata H, Zhang JL, Edgington R, et al. Fluorescent nanodiamonds from molecular diamond seed. In: CLEO: 2015. San Jose, California, Optical Society of America, 2015.
[222] Dahl JEP, Michael Moldowan J, Wei Z, et al. Synthesis of higher diamondoids and implications for their formation in petroleum. Angew Chem Int Ed 2010;49:9881–5.
[223] Tomoki S, Miyazoe H, Saito K, et al. Synthesis of diamondoids by supercritical xenon discharge plasma. Jpn J Appl Phys 2011;50:030207.
[224] Zapata T, Bennett N, Struzhkin V, et al. Organic Nanodiamonds arXiv:1702.06854, 2017.
[225] Wu E, Rabeau JR, Treussart F, et al. Nonclassical photon statistics in a single nickel–nitrogen diamond color center photoluminescence at room temperature. J Mod Opt 2008;55:2893–901.